Exhumation history of the Variscan orogen in western Iberia as inferred from new K-Ar and 40Ar/39Ar data on granites from Portugal

A. Hildenbrand, F.O. Marques, X. Quidelleur, F. Noronha

Exhumation history of the Variscan orogen in western Iberia as inferred from new K-Ar and $^{40}Ar/^{39}Ar$ data on granites from Portugal

Hildenbrand, A.[a], Marques, F.O.[b], Quidelleur, X.[a], Noronha, F.[c]

[a] *Université Paris-Saclay, CNRS, GEOPS, Orsay, 91405, France*

[b] *Universidade de Lisboa, Lisboa, Portugal*

(c) Universidade do Porto, ICT, Porto, 4169-007

Abstract

Exhumation of the roots of collapsing orogens is a key process in the evolution of mountain belts, which is critical for the understanding of orogenic cycles. From new structural analyses, K-Ar and $^{40}Ar/^{39}Ar$ on muscovite, biotite and K-feldspar, and available U-Pb ages, we constrain the cooling and exhumation history of granitic batholiths from the main structural zones of the Variscan orogen in Iberia. We show that: (1) the oldest Ar dated granites (ca. 335 Ma on biotite) record exhumation of gneisses crystallized much earlier (up to ca. 530-510 Ma U-Pb age); (2) granitoids crystallized at ca. 330 Ma record mostly ductile stretching (L-tectonites striking around N-S), consistent with N-S extension (Variscan intra-orogenic collapse); (3) most granites crystallized between ca. 320 and 305 Ma record ductile stretching consistent with deformation along NW-SE to ENE-WSW shear zones during the late-Variscan compression (C3); (4) granites crystallized after 305 Ma record mostly isotropic strain (no visible ductile foliation or lineation), consistent with their emplacement during/after the final collapse of the Variscan orogeny (E2); (5) comparison between Ar ages on micas and zircon U-Pb ages shows two contrasting situations: (i) similar ages, reflecting crystallization and fast cooling, which can be explained by relatively shallow intrusion and/or fast tectonic uplift; (ii) significant difference between U-Pb and Ar ages, supporting crystallization of deeper seated intrusions and their subsequent uplift for several Ma to tens of Ma; (6) thermochronological modelling on K-feldspar supports significant tectonic exhumation in the core of the chain between ca. 315 and 285 Ma, followed by late-stage passive denudation; 7) Late Carboniferous to early Permian tectonic exhumation was accompanied by significant formation of ore-deposits. Tin deposits occur in pegmatites and/or quartz veins associated with muscovite-rich syn-C3 granites and those of tungsten in quartz veins, breccia pipes and skarns associated with the E2 biotite-rich granites.

***Keywords**: Variscan orogeny, western Iberia; $^{40}Ar/^{39}Ar$ and K-Ar dating; $^{40}Ar/^{39}Ar$ thermochronology, Multi-diffusion domain approach (MDD), collapse stage; long-term exhumation*

1. Introduction

The formation of mountain belts involves episodes of granitization at various scales and depths, which contribute to the incremental growth and evolution of the Earth's continental crust (e.g., Hawkesworth et al., 2019). At some point during, between or after the main building stages, orogens may become gravitationally unstable and may experience collapse (e.g., Burg et al., 1994; Rey et al., 2001), denudation, and isostatic rebound, leading to the exhumation of their granitic roots. During the last 20 years, the links between orogenic collapse and crustal exhumation have been extensively investigated through geological, geochronological, and modelling approaches (Vanderhaeghe and Teyssier, 2001; Jadamec et al., 2007; Gerbault et al., 2018; Chardon et al., 2020 and references therein). Some studies have tested the effects of variable viscosity and density of the deep crust during lithospheric extension and identified contrasted modes of exhumation with uplift rates reaching km/Myr (e.g., Korchinsky et al., 2018). Others have studied the influence of in-situ radiogenic heating, shearing, and partial melt generation and migration, which may modify the thermal and mechanical properties of the crust, favouring rapid exhumation, even during ongoing compression (e.g., Gerbault et al., 2018). Nevertheless, the timing and rates of exhumation associated with either collapse tectonics or late denudation by erosion remain, in many cases, insufficiently documented, despite being critical to the understanding of orogenic cycles and ore-deposit formation.

Since the early nineteen forties, geochronological methods based on the natural decay of radioactive elements have been extensively developed to solve a number of problems in Earth Sciences (e.g., Nier et al., 1941; Holmes, 1946; Houtermans, 1946; Roth and Poty, 1985). In the case of old felsic rocks such as granites, the Rb-Sr and U-Pb methods have been widely used to constrain the age of magma production and crystallization at depth. U-Pb on zircon is an especially powerful approach, as the refractory behaviour of this mineral hampers

resetting of the chronometer at high temperature, up to ca. 900 ºC (e.g., Lee et al., 1997; Cherniak and Watson, 2000). While monazite may be sensitive to partial U-Pb age resetting in the presence of hot fluids (e.g., Tartese et al., 2011), magmatic zircons generally keep the memory of various stages of crystallization. These stages can sometimes be resolved at the scale of a single mineral grain through laser-ablation and high-sensitivity ion-probe in-situ measurements of various crystal growths (e.g. Ireland et al., 2008). However, due to its high closure temperature, zircon U-Pb dating does not allow the reconstruction of the cooling history below ca. 900 ºC. Therefore, U-Pb on zircon has been used extensively to constrain successive stages of granite crystallization worldwide. However, it is not suitable to interpret cooling associated with the late-stage collapse and exhumation of mountain belts such as the Variscan orogen in western Iberia.

One way to constrain exhumation rates is to reconstruct the thermal history of batholiths exhumed to the surface by late orogenic isostatic rebound and denudation and compare the differential behaviour of the various portions of an orogen by geochronological and thermochronological investigation. $^{40}Ar/^{39}Ar$ thermochronological approaches based on contrasted diffusion of argon in K-bearing minerals with variable retentivity has been increasingly applied to resolve complex cooling histories (McDougall and Harrison, 1999, and references therein). Variable cooling and exhumation rates have been reported for several orogenic belts, e.g., the Himalayan in Southeastern Tibet (Quidelleur et al., 1997; Harrison et al., 2000), the Pyrenean part of the Hercynian chain (Maurel et al., 2004), the Mesoproterozoic Albany-Fraser Orogen in Western Australia (Scibiorski et al., 2015), or the Eburnean Orogen in the West African Craton (Sagna et al., 2021). In most cases, these studies showed fast cooling and exhumation rates associated with tectonic compression, and much lower cooling rates during late denudation by erosion processes. Such $^{40}Ar/^{39}Ar$ thermochronological approaches therefore provide important insights into the thermal

evolution of the continental crust. Furthermore, they may give valuable information on how, where and when ore deposits may form at depth during the typical development of an orogen, which can also have significant economic impact.

Here we present a K-Ar and $^{40}Ar/^{39}Ar$ geochronological and thermochronological study on granitic batholiths from the two main structural zones of the Variscan Orogen in western Iberia, the Ossa–Morena and Central Iberian zones, and one sample from a parautochthonous complex in the Galicia–Trás-os-Montes Zone (Fig. 1). The combined analysis of minerals with contrasted Ar retentivity and closing temperatures, coupled with available U-Pb data, allows us to reconstruct the thermal and vertical displacement history of the roots of the Variscan Orogen in Iberia during its late stages.

2. Geological background

The Variscan belt was produced by the convergence and collision between Laurussia and Gondwana, after the closure of the Rheic Ocean. The belt is characterized by several geotectonic zones with specific paleogeographic, tectonic, metamorphic and magmatic characteristics (Matte, 1991; Quesada, 1991; Franke, 2000; Simancas et al., 2005; Rosas et al., 2008; Murphy et al., 2016). Subduction with exhumation and retrogression to amphibolite facies of earlier granulite and eclogite rocks took place at ca. 390 Ma (Dallmeyer et al., 1991). It was followed by continental collision at around 370 Ma (Moita et al., 2005a, b). Three main phases of contractional deformation (C1 to C3; Fig. 2) and two extensional events (E1 and E2; Fig. 2) under given metamorphic conditions (M1 to M3) and igneous processes (I1 to I3) are considered responsible for the structures presently observed (e.g. Martínez Catalán et al., 2014).

The Central Iberian, the Galicia–Trás-os-Montes and the Ossa-Morena zones may

correspond to the most internal parts of the Variscan Belt in the Iberian Peninsula (Julivert et al. 1974; Farias et al. 1987). Metamorphic conditions recorded in these zones can be summarized as follows (Ribeiro et al, 2019): the allochthonous massifs of the Galicia-Trás-os-Montes Zone show MP-HT and HP-HT in the Upper Allochthon, HP-LT in the Middle Allochthon, and MP-MT in the Lower Allochthon; the Ossa-Morena Zone records LP-HT in the Parautochthonous, MP-LT and HP-MT in the Allochthon, and HP-HT close to the contact with the Central Iberian Zone, whereas LP-LT metamorphic conditions have been recorded in the South Portuguese Zone. Finally, domal areas of the Central Iberian Zone show P-T paths from LP-LT to MP-HT. These metamorphic conditions reflect the three main stages of the Variscan cycle: (1) LP-HT associated with the Cambrian-Early Ordovician rift stage; (2) HP-LT associated with subduction; and (3) syn-to-post-collisional, MP and LP/HT in the hinterland and foreland fold-and-thrust belts. Thrusting of high-grade rocks to lower crustal levels produced retrogression to lower amphibolite and greenschist facies. Syn- and post-orogenic collapses were also responsible for retrogression to greenschist facies, especially in the core of the Variscan chain where post-orogenic isostatic rebound and denudation brought deep-seated rocks to the surface.

The Central Iberian, the Galicia–Trás-os-Montes and the Ossa-Morena zones are delimited by major shear zones that have played an essential role in the late development and exhumation of the Variscan Orogen in Iberia. The Coimbra-Badajoz-Cordova shear zone is a WNW-ESE mega-shear, which represents an aborted continental rift during Lower Paleozoic times that evolved to a sinistral Variscan flower structure in the upper Paleozoic (Ribeiro et al., 1990). It represents the limit between the Central Iberian and Ossa-Morena zones. The pressures and temperatures reached during the earlier Cadomian Orogeny (Upper Proterozoic) and during the M1 and M2 Variscan phases (Upper Paleozoic) indicate a poly metamorphic evolution of the Badajoz-Cordoba shear zone (Ábalos et al., 1991). The Juzbado–Penalva do

Castelo Shear Zone is an ENE-WSW sinistral shear zone (Iglesias and Ribeiro, 1981), which brought into contact the Figueira de Castelo Rodrigo–Lumbrales Anatectic Complex (S-type granites and migmatites) with low-grade metamorphic units from the autochthonous of the Central Iberian Zone (Ferreira et al. 2019). Exhumation rates associated with non-purely horizontal strike-slip along the Juzbado–Penalva do Castelo Shear Zone has been recently estimated at ca. 800 m/Ma between ca. 315 and 305 Ma (Ferreira et al., 2019).

During the initial steps of decompression in NW Iberia, large volumes of mafic to felsic magmas were generated and emplaced into Neoproterozoic to Palaeozoic sequences of meta-sedimentary and meta-igneous rocks of variable metamorphic grades. Plutonic bodies, based on their geological, petrographic and geochemical characteristics, have been divided into two main groups (e.g., Capdevila et al., 1973; Bea et al., 1999; Ferreira et al. 1987; Dias et al., 2002). A first group consists of two-mica peraluminous granites, considered S-type and resulting from the crystallization of wet peraluminous magmas, whose origin at a mid-crustal level is related to orogenic metamorphism. These granites formed in the core of thermal domes nearly coincident with late Variscan large-scale antiforms. The second group consists of biotite-rich granites (I-Type), which represent the products of complex lower-crustal melting with possible mixture with mantle-derived magmas (e.g. Dias et al., 1998; Orejana et al., 2009; Villaseca et al., 2011). The biotite-rich granites are distributed parallel to ductile shear zones trending NNW-SSE, ENE-WSW and NNE-SSW (Ferreira et al., 1987; Dias et al., 2002; Valle Aguado et al. 2005).

From zircon and monazite U-Pb ages obtained on samples from the Central Iberian and Galicia-Trás-os-Montes zones, the two types of granites have been further divided into several age subgroups. The S-type granites have been divided into three sub-groups: 331-321 Ma, 317-315 Ma and 311-310 Ma. The biotite-rich I-Type granites have been divided into four subgroups: late-E1 (320–315 Ma), syn-C3 (310-305 Ma), and late-C3 and E2 (305-280

Ma) (Dias et al., 1998; Dias et al., 2002; Valle-Aguado, 2005; Neiva et al., 2012; Pereira et al., 2018 and references therein). Considering I-Type magmatism from the Ossa-Morena Zone represented by synkinematic gabbros, granodiorites and tonalites, and older granodiorites from Galicia, we can distinguish an older, generalized episode of I-Type magmatism (early I1) from ca 370 to 335 Ma (Moita et al., 2005a,b; Jesus et al., 2007; Pin et al., 2008; Pereira et al., 2015; Gutiérrez-Alonso et al., 2018).

Several metallogenetic events associated with granites have been recognized (e.g., Neiva, 2002; Mateus and Noronha, 2010). Mostly Sn pegmatites and quartz veins with cassiterite precipitated during the early stage. They are related to S-type granites and are generally associated with quartz, muscovite and arsenopyrite. W (Sn) in quartz-vein deposits are related to late-C3 biotite granites, and W (Mo) quartz veins and stockworks are related to the E2 youngest biotite granites. Fluid inclusion and isotope data show that the biotite-rich Variscan granites (310 to 280 Ma) may also play a different role in the W ore forming processes, because no typical magmatic signature is found in mineralizing fluids, except in the earliest stages responsible for the greisen formation. The heat flow regime supports a late extensive hydrothermal activity throughout the entire crust, involving distinct fluid sources in successively lower P-T conditions along a continuum that provided long-lived hydrothermal systems (Mateus and Noronha, 2010; Noronha, 2017, and references therein).

The age of W and Sn mineralizations is still a matter of debate, due to very scarce geochronological data, which might be biased by late hydrothermal events and alteration processes. In the northeast Galicia-Trás-os-Montes Zone and in the northern part of the Central Iberian zone, deformed Sn-pegmatites associated with cassiterite deposits in the exo-contact of a syn-C3 granite were dated at 307 ± 3 Ma by Rb-Sr (Priem and den Tex, 1984), whereas recent U-Pb ages on cassiterite range from 331 ± 5.6 to 310 ± 6 Ma (Zhang et al., 2019). U-Pb ages on minerals of the columbite-tantalite group from pegmatites in the exo-

contact of a late-C3 biotite-muscovite granite yielded ages of 301 ± 4 and 316 ± 9 Ma (Lima et al., 2013). $^{40}Ar/^{39}Ar$ ages on muscovite from similar non-deformed veins of pegmatite and quartz including lithium minerals and fine cassiterite near the Portugal-Spain border recorded two age groups around 305 and 295 Ma (Vieira et al., 2011). Further to the northwest, the hydrothermal systems of W (Mo) at Borralha record post-magmatic cooling associated with the youngest E2 biotite granites in the Galicia-Trás-os-Montes Zone. An $^{40}Ar/^{39}Ar$ age of 286.8 ± 1.2 Ma on muscovite probably reflects secondary formation from magmatic biotite or feldspar alteration, while an age of 280.9 ± 1.2 Ma in sericite may date the age of greisen alteration (T~300 ºC). Ages of 281.3 ± 1.2 and 277.3 ±1.3 Ma were obtained on muscovite (selvage) crystallized adjacent to molybdenite rich veins (Bobos et al., 2019), in very good agreement with the previous zircon U–Pb age of 280 ± 5 Ma for the Gerês E2 biotite granite. A younger K-Ar age of 273 ± 1.1 Ma was obtained on feldspar resulting from hydrothermal alteration of the Gerês granite (Jaques et al., 2016).

At Panasqueira (southern part of the Central Iberian Zone) the largest W (Sn) deposit in the Iberian Peninsula is spatially associated with a greisen cupola. $^{40}Ar/^{39}Ar$ ages on muscovite from quartz veins and greisen constrain fluid circulation between 296.3 ± 0.8 and 291.6 ± 0.8 Ma (Snee et al., 1988). The earliest hydrothermal event (tourmalinization) was recently dated at 305.2 ± 5.7 Ma by U-Pb on rutile (Carocci et al., 2019) and at 303.0 ± 3.3 and 301 ± 4.2 Ma by U-Pb on cassiterite (Zhang et al., 2019). In addition, a U-Pb age of 296.3 ± 4.2 Ma was obtained on apatite from the Panasqueira greisen, which is similar to a U-Pb age of 294.5 ± 5.3 Ma obtained on apatite from the mineralized veins (Launay, 2018). All these data are seemingly contradictory. This may be the result of the complex and long history typical of a large deposit that implies successive reopening of mineralized veins.

3. Methods

3.1. Sampling strategy and description

Forty-five granitic outcrops in Central and Northern Portugal were studied and sampled, in order to measure the visible strain and assess the timing of pluton emplacement, the age of the main deformation episodes, and the exhumation of the roots of the Variscan orogen in western Iberia. Deformation markers (faults, foliation, mineral lineation) were measured as trends, providing a qualitative estimation of strain and its dominant orientation, as reported in Table 1. Sampling initiated in the south near the city of Évora and progressed northwards along a SSE-NNW transect across the Ossa-Morena and Central Iberian zones, ending in the Galicia-Trás-os-Montes Zone. Only twelve out of the forty-five samples collected were dated. In each zone, representative samples were selected for argon geochronological and thermochronological studies based on their freshness and location in the orogen, as well as type and degree of strain (Table 1). The analysed samples are reported on a synthetic map showing the main Variscan and pre-Variscan chrono-stratigraphic units (Fig. 1). For each sample, a detailed description of the geological unit such as given in the Geological Map of Portugal scaled at 1/500 000 (LNEG, 1992) is also provided (Table 1, Supplement 1).

The five samples collected in the Ossa-Morena Zone (Fig.1) include pre-, syn- and post-orogenic granitoids (*sl*), ranging from highly deformed to un-deformed. Near Évora, we sampled a pervasively foliated, biotite-rich granitoid (sample 107D) referred to as "Proterozoic rocks partially migmatized during the Variscan Orogeny" (Table 1). Slightly further East, near Vendinha, we collected a less-deformed granite (sample 107G), described as a "syn-orogenic tonalite" (Fig. 1, Table 1). On the geological map (LNEG, 1992), both outcrops are part of an elliptical large body roughly elongated NW-SE, which may have (re-) crystallized during a main deformation stage of the Variscan orogeny. Further north, sample

107J, collected near Pavia village, is from a weakly deformed two-micas porphyroid granite. It is mapped as cutting Variscan tonalites and should therefore be younger; however, the contact is unclear and seems to be made up of small faults. In any case, this granite is also mapped as "orogenic" in the geological map (LNEG, 1992, Table 1). Further north, near Campo Maior, another "orogenic" plutonic body mapped as anorthosite gabbro (though containing biotite) was also collected (sample 107P). Finally, an undeformed porphyroid granite cutting previous units, referred to as late-Variscan in the geological map (LNEG, 1992), was collected close to the northern boundary of the Ossa-Morena Zone near the Monforte village (sample 107K).

The six studied Central Iberian Zone granites also range from deformed to undeformed. Sample 107T is from an undeformed granite collected near the Alpalhão village, close to the boundary between the Central Iberian and Ossa-Morena zones (Fig. 1). Sample 107X is from an isolated biotite-bearing quartz-diorite batholith near the Fundão town, considered either as a "syn-tectonic" granite (LNEG, 1992), or a pre-Variscan Ordovician granite and tonalite from zircon U-Pb ages around 478 ± 2 Ma reported more recently by Antunes et al. (2012). A few tens of kilometres further to the NE, near the border with Spain, we sampled a biotite granite with minor muscovite (sample 107AC), which is cut by E-W to NE-SW normal faults (Table 1), thus pointing to a late tectonic (regional?) event with a N-S to NW-SE extensional component. We note that the NE direction is also marked by numerous felsic dykes in the area (Table 1). A few km to the north, deformed granites and gneisses are also elongated along the ENE-WSW direction, but they are mapped as emplaced during early deformation events. We sampled a lenticular gneiss with minor muscovite (sample 107AH2), and a so-called "syn-tectonic granite" (sample 107AJ). The latter is affected by two distinct vertical foliation planes (S-C mylonite), one oriented N135 (S-type) and the other N090 to N100 (C-type), with a 15-N100 stretching lineation and shear criteria indicating left-lateral

kinematics (Table 1). In contrast, many structures with a dominant NW-SE orientation occur further west. These include a NW-SE elongated deformed granite (sample 107AN) emplaced during E1 stage, which we collected at Lamego town. The granite is cut by a major NW-SE fault zone that can be followed on the geological map for several tens of kilometres (Fig. 1).

Finally, on the opposite block of this fault, we collected an undeformed porphyroid monzonite granite (sample 107AS) near Guimarães city. This sample does not belong to the Central Iberian Zone stricto sensu, it is a granite intruded into the Galicia-Trás-os-Montes Zone.

3.2. K-Ar and $^{40}Ar/^{39}Ar$ dating

Careful examination of thin sections (Supplementary Fig. 1) was conducted to constrain the main petrographic characteristics of the samples and ensure that they did not undergo significant weathering, which is critical for subsequent reliable argon dating. All the samples are granitoids s.l. (granodiorites, fine-grained granites, porphyroid granites, aplites dykes, orthogneisses), with structures and textures ranging from equant, isotropic and undeformed to the naked eye, to strongly foliated (S-tectonite) or conspicuously lineated (L-tectonite). The mineralogy is dominated by K-feldspar ± quartz ± mica (biotite, or muscovite, or both), and includes some accessory minerals such as apatite, titanite, oxides and occasionally tourmaline.

After crushing and sieving to a grain size in the interval 250 - 500 μm, the various K-bearing mineral phases were extracted by means of magnetic separator and heavy liquids. Whenever possible, either two or three distinct mineral phases were selected for a given sample. For two-mica granites (107J, 107T and 107AC), especially, muscovite, biotite and K-

feldspar were extracted. Such separation is essential to check for internal consistency within the sample and evaluate whether the ages measured may reflect crystallization age or cooling, as these various phases have different Ar retentivity with respect to temperature. As such, they can be used to carry out a thermo-chronological study aimed at constraining the path of the samples through the different isotherms, and thus discuss the thermal history in terms of exhumation and/or potential partial resetting during thermal events.

The K-Ar and $^{40}Ar/^{39}Ar$ analyses were carried out at the GEOPS Laboratory in Orsay (France). Details on the K-Ar analytical procedure and its applicability can be found elsewhere (Gillot et al., 2006). For each mineral phase, K was measured at least twice by flame absorption photometry, and compared with standards MDO-G (Gillot et al., 1992) and BCR2 (Rackzek et al., 2001). The K-value is the arithmetic average of independent measurements and is considered final when the relative standard deviation (1σ) is lower than 1%. The $^{40}Ar/^{36}Ar$ isotopic composition was measured on a 180° sector multi-collector mass-spectrometer similar to the one described in Cassignol and Gillot (1982) and Gillot and Cornette (1986). At least two independent Ar measurements were completed on both biotite and muscovite and the final K-Ar age is calculated as the weighted-mean of individual determinations consistent at the 1σ level. One Ar determination was conducted in K-feldspar of the samples for preliminary purposes, as K-Ar ages on such phases generally provide inconclusive information regarding granite crystallization age at depth due to their poor Ar retentivity at high temperature (e.g. Sagna et al., 2017). However, K-feldspar can be used to achieve a thermochronological analysis through step-heating $^{40}Ar/^{39}Ar$ (see next section, and Lovera et al., 1997; Sagna et al., 2021).

The $^{40}Ar/^{39}Ar$ analyses were performed using the multi-collector mass-spectrometer and procedure described by Coulié et al. (2004). Aliquots of the samples (30 to 80 mg) were first irradiated along with fluence monitors during 60 h in the Corvallis Triga reactor

(Radiation Center, Oregon state University, USA), using the CLICIT facility. Gas extraction of the samples was completed by step heating with a high frequency furnace. A Nd-YAG laser (1064 nm) was used to fuse 20 mg aliquots of the Heidelberg biotite international standard HD-B1 (Fuhrmann et al., 1987), in order to determine the J factors based on the age of 24.18 Ma for HD-B1 (Schwartz and Trieloff, 2007). The mass discrimination was corrected using a linear law applied to analyses of air aliquots measured with the same ^{40}Ar signal intensity as that measured for a typical step. The K isotopic ratio and ^{40}K decay constants of Steiger and Jäger (1977) were used. It has been demonstrated that $^{40}Ar/^{39}Ar$ ages with 0.1% of analytical relative precision can be reached with our instrument (e.g. Ricci et al., 2013). However, as $^{40}Ar/^{39}Ar$ dating is relative to the flux monitor age, this represents the main limiting factor for the accuracy of this technique (Kuiper et al., 2008). It should be noted that differences of about 1% exist for the admitted ages of commonly used fluence monitors such as Fish Canyon Tuff Sanidine and HDB-1. These differences can be explained by inter-laboratory biases, or by the presence of previously undetected ^{39}Ar recoil (Phillips et al., 2017). Therefore, the $^{40}Ar/^{39}Ar$ total age uncertainties from the present study include a systematic error of 1% for the J-Factor determination.

3.3. $^{40}Ar/^{39}Ar$ thermochronology

The multi-diffusion domain approach (MDD) was used here to reconstruct the thermal history recorded in K-feldspars of key samples (107J, T, X, AC and AS). The MDD approach relies on the hypothesis that diffusion of Ar occurs similarly in nature as in the laboratory and that diffusion of Ar in K-feldspar can be modelled by a discrete distribution of non-interacting domains (Lovera et al., 1989; Lovera, 1992). Using the laboratory $^{40}Ar/^{39}Ar$ step-heating measurements, diffusion parameters (i.e. activation energy and frequency factor) can be

329 recovered from the Arrhenius diagram built using the degassing systematics of reactor-
330 produced $^{39}Ar_K$ (Lovera et al., 1989). In the case of our samples, the first degassing steps did
331 not allow a precise determination of the activation energy (see Supplementary Figures 1 and
332 2) and hence the value of 46 ± 6 kcal.mol^{-1} typically used for K-feldspar was imposed
333 (Lovera et al., 1997). Monotonic cooling histories can be computed using inverse modelling,
334 hence without an a-priori thermal history. On the other hand, a forward modelling approach
335 with an input thermal history is necessary when post emplacement re-heating is considered. In
336 our case, forward modelling was achieved using constraints obtained from biotite and
337 muscovite (closure temperatures of 300 °C and 350 °C, respectively; McDougall and Harrison,
338 1999), and available U-Pb ages on zircons (T > 650 °C). The cooling history that best
339 reproduces the degassing age spectra is shown for each sample (Supplementary Figure 3).
340 Finally, we tested the potential effects of a thermal event, by imposing moderate re-heating
341 (RH) below a temperature of 300 °C (closure temperature of biotite) at various epochs (200
342 Ma, 240 Ma, and 260 Ma, Supplementary Fig. 4) for our best-characterized sample (107AC).

343

344 **4. Results**

345 4.1. K-Ar and $^{40}Ar/^{39}Ar$ dating

346 The new K-Ar ages (Table 2) range from 264 ± 4 to 335 ± 3 Ma. For samples with 3
347 mineral phases analysed (J, T, AC), K-Ar ages on biotite and muscovite are mutually
348 indistinguishable within the range of uncertainties. Preliminary ages on K-feldspar for these
349 samples are, however, systematically younger by more than 20 Ma, and up to 30 Ma (Table 2).
350 Such discrepancy is significant, as it represents a relative offset of ca 10%. Sample 107X, for
351 which only two phases were available, shows a similar behaviour, with K-Ar ages of 288 ± 4
352 and 264 ± 4 Ma obtained on biotite and K-feldspar, respectively.

353 $^{40}Ar/^{39}Ar$ age spectra obtained during incremental step-heating on biotite and
354 muscovite produced relatively well-defined plateaus (Fig. 3), with more than 50% of ^{39}Ar gas
355 released and a minimum of three steps, all steps included in the plateau being consistent at the
356 2σ level (e.g., Fleck et al., 1977; McDougall and Harrison, 1999). We note, however, that
357 biotites from samples 107J and 107X do not meet these criteria, due to the presence of steps
358 with older apparent ages at relatively high temperatures, which may reflect the contribution of
359 inclusions of incompletely reset accessory minerals, e.g. small oxide grains. Such minerals,
360 along with apatite, frequently occur in the samples (as observed in thin section). However,
361 such effect appears limited, as revealed by the overall flat shape of the spectra. Similar outlier
362 steps also occur for biotites from samples 107T, 107AC and 107AN, but in these cases they
363 do not preclude the definition of a plateau. The effect is negligible as plateau ages and
364 integrated ages for these samples are fully consistent. In other words, removing the outliers
365 would define a more robust plateau, i.e. calculated from a higher ^{39}Ar content, but with
366 negligible effect on the total gas age. The spectra on muscovite are even flatter and provide
367 similar plateau and integrated ages (Fig. 3). They also yield comparable results with the
368 $^{40}Ar/^{39}Ar$ obtained on biotite of the same samples and are fully compatible with the K-Ar ages
369 (Fig. 4).

370 In contrast, the spectra obtained during incremental heating of K-feldspar (Fig. 5)
371 from the various samples show a clear stairway shape, typical of either a long gradual cooling
372 history or thermal disturbance (re-heating; McDougall and Harrison, 1999).

373

374 4.2. $^{40}Ar/^{39}Ar$ thermochronology (MDD modelling)

375 Inverse modelling (monotonic cooling) and forward modelling give similar results for
376 the feldspars of samples 107AC and 107AS (Fig. 6 and Supplementary Figs. 2 and 3). This

confirms the relevance of the value of 46 Kcal/mol used for activation energy (Lovera et al., 1997) for all our samples. The cooling histories (300-250 Ma) imposed for forward MDD modelling that best fit $^{40}Ar/^{39}Ar$ age spectra for feldspars from our samples 107J, 107X, 107AC, and 107AS (see Supplementary Figure 4) are shown on Figure 7. While sample AS records a relatively early and fast temperature drop after 300 Ma, samples J, X and AC show a much longer cooling history. The latter two samples especially, which belong to the Central Iberian Zone, record temperatures exceeding 200 °C until ca. 250 Ma.

Results of our test regarding a possible re-heating event are shown on Supplementary Figures 5. The first two tests (re-heating at 200 Ma and 240 Ma) fail to reproduce any of the apparent ages of the degassing spectra. Conversely, a re-heating of about 275 °C at 260 Ma (blue line in Supplementary Figure 5C) fits most of the spectra relatively well, but is not substantially better than the simplest hypothesis of monotonic cooling since 300 Ma.

5. Discussion

Overall, the new $^{40}Ar/^{39}Ar$ ages (Table 3 and Figs. 5-6) confirm the validity of the new K-Ar ages and show that none of our samples have undergone significant thermal disturbance above the closure temperature of biotite (i.e. ca. 300 °C). By extrapolation, this also supports the validity of the K-Ar ages on biotite for samples not analysed with $^{40}Ar/^{39}Ar$, especially 107D and 107G (see also comparison with available U-Pb ages in Supplement 1). In contrast, the abnormally young K-Ar ages systematically obtained on K-feldspars from our samples, and the stairway shape of the degassing $^{40}Ar/^{39}Ar$ spectra (Fig. 5), both reflect incomplete Ar retention. Our MDD modelling test for re-heating does not support significant re-opening of the Ar system due to re-heating (Supplementary Fig. 5), ruling out significant contribution from large, generalized thermal events, such as the plume-related emplacement of the Central

401 Atlantic Magmatic Province (CAMP) ca. 200 Ma ago (e.g., Marzoli et al., 1999; Nomade et
402 al., 2007). This is consistent with recent apatite fission-track data obtained on two of our
403 samples (107T and AC), which show no detectable temperature increase beyond 60-110 °C
404 during the last 250 Ma (Barbarand et al., 2021). Therefore, the thermal histories recorded by
405 the various mineral phases of our various samples (muscovite, biotite, and K-feldspar) most
406 likely reflect monotonic cooling at various rates in relation to granite emplacement and
407 exhumation.

408

409 *5.1. Syn- and post-deformation episodes of granite production: where and when?*

410 Comparison of the new K-Ar and $^{40}Ar/^{39}Ar$ ages on biotite and muscovite with
411 available U-Pb data on zircon inferred to represent true crystallization age of the granites is
412 given for each sample in Supplement 1 and shown on Fig. 8. In summary, the new K-Ar and
413 $^{40}Ar/^{39}Ar$ ages on micas are either similar to or slightly lower than existing U-Pb ages on
414 zircon. In the former case, the new ages are consistent with U-Pb crystallization ages, despite
415 the great difference in closure temperature: up to ca. 900 ºC for U-Pb in zircon (Lee et al.,
416 1997), compared to ca. 350 or ca. 300 ºC for Ar in muscovite or biotite, respectively
417 (McDougall and Harrison, 1999). We thus infer rapid cooling. Rapid cooling can take place in
418 two situations: granite emplacement at relatively shallow crustal level (T < 300 °C), or granite
419 emplacement during very fast uplift. A U-Pb age significantly older than the Ar age indicates
420 a different thermal history, which can be explained by crystallization at greater depth (T >
421 closure temperature of muscovite), followed by relatively slow cooling.

422 Plotting the new mica K-Ar and $^{40}Ar/^{39}Ar$ ages on a structural map of Portugal (Fig. 9)
423 allows several main patterns to be distinguished, which are summarized as follows:

424 - At the scale of the whole investigated area, the new ages decrease globally from S to N, i.e.

425 from 335 ± 3 Ma (sample 107D) to 290 ± 4 Ma (107AJ). The youngest age (sample 107X, ca.
426 285 Ma), however, departs from the general trend.- Two main age groups occur according to
427 the two main tectonic zones. Samples in the Central Iberian Zone are constrained between
428 305 and 285 Ma, whereas samples from the Ossa-Morena and Galicia-Trás-os-Montes zones
429 are dated in the range 335-305 Ma. Regarding the Galicia- Trás-os-Montes Zone, however, a
430 sampling bias is possible, as only one sample (107AS) has been analysed here, whereas U-Pb
431 ages as young as 280 ± 5 Ma have been reported for E2 biotite granites in this area (Mendes
432 and Dias, 2004). Older granites in Galicia and northern Portugal have been dated around 347-
433 310 Ma (Martínez Catalán et al., 2014; Gutiérrez-Alonso et al., 2018), which is comparable to
434 the age of synkinematic gabbros, granodiorites, and tonalites in the Ossa-Morena Zone.
435 However, the oldest granites from Galicia and northern Portugal are associated with Variscan
436 shear zones, whereas deformed plutonic bodies in the southern Ossa-Morena Zone show
437 tholeiitic to calc-alkaline affinities associated with subduction processes (e.g., Pereira et al.,
438 2015).

439 - Within each of the zones investigated here, the oldest K-Ar and $^{40}Ar/^{39}Ar$ ages are obtained
440 on deformed granites. In the Ossa-Morena Zone, the rocks with greater deformation occur
441 along the NW direction and are dated in the range 335-310 Ma, whereas undeformed granites
442 cross-cutting previous units (samples 107K and 107P) yield K-Ar and $^{40}Ar/^{39}Ar$ ages closer to
443 305 Ma. In the Central Iberian Zone (and Galicia-Trás-os-Montes Zone, sample 107AS) ages
444 around 305-300 Ma are obtained on samples along major tectonic structures with a similar
445 NW-SE trend. In addition, a group of rocks with significant superimposed late deformation
446 along the NE-SW to E-W direction in the Central Iberian Zone (107X, 107AC, 107AH2) is
447 here dated around 295-285 Ma.

448 - Strongly deformed samples from the Ossa-Morena Zone (107D and 107G) show similar U-
449 Pb and K-Ar ages, supporting very rapid cooling after (syn-tectonic) crystallization. For these

samples, steep pervasive foliation and mineral lineation striking N160 and N170 (samples 107D and 107G, respectively) suggest an important event of ductile stretching ca. 335-325 Ma ago.

- Undeformed samples from both the Ossa-Morena and the Galicia-Trás-os-Montes zones also show very similar U-Pb, K-Ar and $^{40}Ar/^{39}Ar$ ages, but the lack of obvious syn-kinematic (ductile) crystallization for these samples supports granite emplacement and rapid cooling at a shallow level around 305 Ma.

- In contrast, an offset from a few Ma up to 30 Ma is observed between U-Pb and the new K-Ar and $^{40}Ar/^{39}Ar$ ages for our deformed samples from the Central Iberian Zone and also for the sample 107J from the Ossa-Morena Zone. This suggests that the crystallization of these granites constrained by U-Pb ages occurred relatively deep. Then, their subsequent cooling occurred over millions of years at a slower rate, as constrained by the $^{40}Ar/^{39}Ar$ ages. This may be due to the position of the sampled granites closer to the axis of the chain, where important deformation and thickening of the crust occurred, leaving the corresponding rocks at depth for a relatively long period of time before their exhumation by either tectonic processes or late erosion and isostasy.

5.2. Exhumation rates and processes

The long-lasting thermal history recorded by some of our samples (several Ma difference between U-Pb and Ar ages) is unlikely to result solely from in-situ cooling at a fixed vertical position after granite emplacement/crystallization. It has been shown that a batch of liquid granitic magma of a few cubic kilometres emplaced at depths around 6-8 km (e.g., Vigneresse, 1999) cools down to around 300 °C on timescales of only a few tens of thousands of years (e.g., Nabelek et al., 2012). Such period is far shorter than the uncertainty

of both U-Pb, K-Ar and $^{40}Ar/^{39}Ar$ ages. On the other hand, a long-lasting thermal evolution exceeding a few Ma more realistically records the successive positions of the granitic bodies at various depths. Therefore, monotonic cooling rates can be reasonably interpreted in terms of exhumation rates. For consistency with earlier works on batholiths from Portugal, we will use an average geothermal gradient of 42 °C/km (Pereira et al., 2017) throughout the period of interest. From the reconstructed thermal history of our 4 samples (107J, X, AC and AS, Fig. 7), we can draw a synthetic cartoon showing the position of the granites along a main N-S cross-section passing through the Ossa-Morena, Central Iberian and Galicia-Trás-os-Montes zones at decreasing ages (Fig. 10):

- At 300 Ma, our samples from the Ossa-Morena (107J) and Galicia-Trás-os-Montes (107AS) zones were already located at shallow depths ($T < 300$ °C, $d \approx 7$ km), whereas samples from the Central Iberian Zone (107X and 107AC) had just crystallized at a deeper structural level ($d > 15$ km).

- Between 300 and 285 Ma, sample 107J experienced relatively modest cooling (2 °C/Ma) and slight uplift (ca. 1 km), supporting a rather stable character of the central part of the Ossa-Morena Zone, which was structured and tectonically exhumed by intra-orogenic collapse well before (no evidence for significant deformation after 325 Ma). Over the same period, feldspars of our three other samples (107X, AC and AS) show relatively rapid cooling (12-25 °C/Ma), corresponding to relatively fast vertical exhumation (300-600 m/Ma), which supports a significant influence of tectonics. In the Central Iberian Zone, rates of tectonic exhumation have been recently estimated from U-Pb ages obtained on zircon and apatite in deformed granites sampled just to the North of an ENE-WSW trending main sinistral shear zone (Juzbado-Penalva do Castelo Shear Zone), which was active during the late-Variscan C3 contractional stage (Ferreira et al., 2019). From the different closure temperatures of zircon and apatite (ca. 830 °C and 480 °C, respectively), the authors calculated cooling rates ranging

499 from 0 to 35 °C/Ma, which, for a geothermal gradient of 42 °C/km (Pereira et al., 2017), gives
500 an exhumation rate of up to 800 m/Ma between ca. 315 and 305 Ma. Our deformed gneissic
501 sample 107AH2, also located north of the Juzbado-Penalva do Castelo Shear Zone, yields a
502 K-Ar biotite age of 294 ± 4 Ma, for an estimated U-Pb zircon crystallization age of 313-317
503 Ma (Table 1 and Supplement 1). Considering closing temperatures of 830 °C (Ferreira et al.,
504 2019) and 300 °C for zircon and biotite, respectively, sample 107AH2 cooled at a rate of 25
505 ºC/Ma over the period 315-295 Ma, corresponding to a vertical exhumation rate of 500-800
506 m/Ma. These values are similar to the rates obtained from MDD modelling on feldspars of
507 deformed samples 107X and 107AC, between 300 and 285 Ma. Altogether, these data point
508 to relatively fast cooling and exhumation associated with significant tectonic deformation in
509 the Central Iberian Zone before 285 Ma. It should be noted that samples 107AH2 and 107AC
510 are located north and south of the Juzbado-Penalva do Castelo Shear Zone, respectively (cf.
511 Fig. 9). This confirms the dominant trans-current movement in the Juzbado-Penalva do
512 Castelo Shear Zone, although with a possible small vertical movement as suggested by
513 Ferreira et al. (2019).

514 - Between 285 and 275 Ma, samples 107J and 107X experienced modest cooling and
515 exhumation (5 to 8 °C/Ma, corresponding to 1 to 2 km uplift), likely due to denudation and
516 isostatic rebound, whereas samples 107AC and 107AS do not show any significant sign of
517 cooling/uplift. This period coincides with the emplacement of late-stage (post-orogenic)
518 granites and mineralization events, which marked the end of the Variscan cycle.

519 - Between 275 and 250 Ma, most of our samples appear stable and remain close to the surface
520 (d = 3-5 km), except for sample 107AC, which shows slight cooling (4 °C/Ma) and uplift
521 from ca. 7 km to 4 km depth. This time lapse may mark the progressive onset of the alpine
522 cycle, but no obvious imprint is recorded by the feldspars of the four tested samples.

5.3. Mineralization processes

A full characterization of ore forming processes is beyond the scope of the present paper. However, our new data, combined with previous studies (Mateus and Noronha, 2010; Noronha, 2017), provide a general and comprehensive view on the timing of main mineralization events and their genetic link with granite emplacement and exhumation.

Fluid inclusion studies in W-Sn hydrothermal vein deposits suggest that most of the fluids that migrated in the upper crust at the end of the Variscan orogeny were mixed with surface waters during the decrease in the P-T conditions (Boiron et al., 1996). In mineralized systems, aqueous-carbonic fluids with trapping conditions of P (50 to 150 MPa) and T (300 to 520 °C) associated with cassiterite and wolframite are contemporaneous with a thermal peak related to granite emplacement (Noronha et al., 1999; 2013). A continuous input of superficial waters in the system and the decreasing of the P-T conditions yields a dilution of fluids with a rise in density. The fluid-related sulphide deposition ($30 < P < 100$ MPa and $T < 370$ °C) are aqueous with low salinity and assumed to result from the mixing of modified fluids with meteoric fluids. Some more saline and colder fluids (brines) have been recognized in quartz veins related to hydrothermal alterations associated with late-Variscan Pb mineralizations (Marques de Sá et al., 2019). This cycle suggests that fluids are related to granite crystallization relatively deep and that their subsequent cooling occurred at a slow rate, over millions of years, justifying an important role of magmatism in the ore forming processes supplying heat to drive the mineralizing system. The late exhumation can justify the input of surficial fluids into the system. This situation is compatible with the case in which the U-Pb age is significantly older than the Ar age, which can be explained by crystallization at greater depth ($T >$ closure temperature of muscovite) followed by relatively slow cooling. The

emplacement of the granitic rocks and the uplift and general decompression of the Variscan units were the main driving forces for fluid migration, as magmatic fluids are relatively scarce in the mineralizing systems.

In contrast, undeformed granites with similar K-Ar, $^{40}Ar/^{39}Ar$ mica ages and U-Pb zircon ages record rapid cooling. In such case, granite emplacement occurred at relatively shallow crustal levels, and was responsible for contact metamorphism and skarn type breccia pipes deposits (metasomatic deposits).

5.4. Broader implications

Our data complement existing studies on the Variscan Orogen and others, and provide significant new insights into the complex vertical motions and exhumation mechanisms in evolving orogens.

Several episodes of exhumation, sometimes diachronic, have been previously proposed for the main portions of the Variscan Orogen in central and western Europe:

(1) Early tectonic exhumation associated with subduction of the hyper-extended margins of Gondwana. This episode, which lasted from middle to late Devonian (see recent synthesis in Vanderhaegen et al., 2020), was not investigated in the present study.

(2) Early to mid-Carboniferous exhumation during/after continental collision. This episode is generally attributed to significant thickening of the crust and subsequent collapse of the chain. It has been recorded by metamorphic and syn-orogenic magmatic rocks from several Variscan massifs: in Brittany (Gumiaux et al., 2004), in the French Massif Central (e.g., Gébelin et al., 2009; Chardon et al., 2020), in the western part of the Maures-Tanneron Massif (Morillon et al., 2000; Gerbault et al., 2018), in the Vosges Massif (Boutin et al.,

570 1995), in the Bohemian Massif and the western Carpathians (e.g., Bues et al., 2002; Franek et
571 al., 2011; Moussalam et al., 2012; Vacek et al., 2019), and in Iberia (e.g., Rosas et al., 2008;
572 Pereira et al., 2017; Gutiérrez-Alonso, 2018; Ferreira et al., 2019; this study). Proposed
573 exhumation mechanisms include large-scale crustal folding and thrusting, transcurrent motion
574 along shear zones, upward flow of buoyant material, and horizontal spreading along crustal
575 detachments. Our new data on deformed samples from the Ossa-Morena Zone record ductile
576 stretching consistent with N-S extension and very fast uplift, here interpreted as a brief
577 episode of Variscan intra-orogenic collapse around 335-330 Ma (E1 in Fig. 2). In contrast,
578 most granites crystallized between ca. 325 and 305 Ma record ductile stretching and
579 significant uplift consistent with deformation along NW-SE to ENE-WSW shear zones during
580 late-Variscan compression (C3). This supports a significant stress change around 330-325 Ma,
581 at least in this part of Iberia, and suggests that contrasted styles of tectonic deformation
582 (extensional vs transpressional) can equally promote significant rapid uplift/exhumation of the
583 lower crust within only a few Ma. These characteristics may additionally constitute a unique
584 witness of a (diachronic?) change in deformation style from extension-dominated to
585 transpression-dominated across the orogen.

586 (3) Late Carboniferous to early Permian tectonic exhumation associated with the final
587 gravitational collapse of the Variscan Orogen (e.g., Burg et al., 1995, Marques et al., 2002).
588 This stage involved significant crustal thinning through transtensional and extensional
589 deformation along low-angle detachments. Related decompression triggered significant
590 partial melting of the lower crust (anatexis), presently witnessed by migmatite domes and
591 late-orogenic anatectic granites, often intruded by younger post-orogenic granites. These
592 various types of rocks are presently exposed in many places of the Variscan Orogen, e.g., in
593 the South Armorican Domain (Turillot et al., 2011; Ballouard et al., 2015), in the French
594 Massif Central (Chardon et al., 2020; Vanderhaeghe et al., 2020), in Italy (Ayuso et al., 1994),

595 in the Pyrenees (Maurel et al., 2004), and in Iberia (references above; this study). In most
596 instances, available U-Pb, Rb-Sr and $^{40}Ar/^{39}Ar$ ages on amphiboles and micas suggest
597 significant exhumation until at least 290 Ma (Turillot et al., 2011; Chardon et al., 2020).
598 Nevertheless, $^{40}Ar/^{39}Ar$ data on feldspars are very scarce (e.g. Maurel et al., 2004), limiting
599 our knowledge of subsequent shallow exhumation dynamics at the full scale of the orogen.
600 Our new MDD data on samples 107X and 107 AC from the Central Iberian Zone have
601 recorded significant cooling and exhumation between ca. 300 and 285 Ma. While the period
602 300-295 Ma coincides with late sinistral movement along main shear zones in the Central
603 Iberian Zone (see previous point), exhumation in the range 295-285 Ma may more
604 realistically be related to (the onset of?) transtension and extension processes associated with
605 the final collapse of the chain (E3 in Fig. 2). Such possibility is supported by the presence of
606 dyke swarms with sharp contacts (chilled margins) and brittle faults with normal-dextral
607 kinematics affecting our samples 107 X and 107AC, respectively (see Table 1).

608 (4) Late exhumation driven by either Alpine tectonics (*sl),* or denudation by erosion
609 processes. The thermal influence of the Alpine cycle related to Triassic early extension and
610 opening and closure of the Tethys has been recorded for instance in the central Serbo-
611 Macedonian Massif in the Carpathians (e.g., Antic et al., 2017). Regarding Iberia, recent
612 Apatite Fission Track (AFT) data on siliciclastic sediments filling Mesozoic basins along the
613 western margin of Iberia support significant uplift of the Newfoundland-Iberia rift shoulder
614 following the opening of the Atlantic at ca. 150 Ma (Barbarand et al., 2021). However, the
615 granites studied here are located further to the East of the margin. In fact, AFT data on our
616 samples 107T and 107AC show continuous cooling since granite emplacement. Our new
617 MDD data on K-feldspars of the four tested samples from the various structural zones support
618 very slow cooling rates (only a few °C/Ma) between 275 and 250 Ma. This is consistent with
619 average cooling rates of 1 °C/km recorded by K-feldspar from the weakly deformed Mont-

620 Louis granite in the Eastern Pyrenees, though the latter rate has been estimated on a much
621 larger temporal window between 295 and 60 Ma (Maurel et al., 2004). The relatively low
622 cooling rates here obtained for the Central Iberian Zone are interpreted as evidence for slow
623 exhumation driven by passive denudation and isostatic re-adjustment immediately after the
624 collapse of the orogen.

625 To summarize, our data recorded the successive stages of exhumation associated with
626 the main steps of evolution of the Variscan belt following early continental collision. The
627 combined use of new structural data, K-Ar and $^{40}Ar/^{39}Ar$ ages on micas, and K-feldspars
628 thermochronology, along with available U-Pb ages support a major role of the various
629 tectonic processes over a cumulative period of about 50 Myr, followed by much slower
630 evolution driven by passive denudation. Such a scenario is consistent with cooling histories
631 depicted by similar geochronological and $^{40}Ar/^{39}Ar$ thermochronological studies on other
632 orogens. For the Cretaceous Gangdese batholith emplaced in Southeastern Tibet during
633 Tethys subduction, mean rates of about 25°C/Myr have been recorded from about 900 to
634 300 °C (Quidelleur et al., 1997), in relation to the high slip rate of 7 mm/yr modelled for the
635 Gangdese Thrust (Harrison et al., 2000). Such fast tectonic exhumation rates have also been
636 inferred for older orogens. During the Mesoproterozoic Albany-Fraser Orogen (Western
637 Australia), rapid exhumation driven by transpressional tectonic activity induced high cooling
638 rate, up to 30 °C/Myr from 585 to 365 °C (Scibiorski et al., 2015). For the Eburnean Orogen
639 in the West African Craton, Paleoproterozoic granites record relatively high cooling rates up
640 to 20 °C/Myr from 900 to 300 °C (Sagna et al., 2021). In contrast, much lower cooling rates
641 of only a few °C/Myr have been inferred for the Grenville Orogen over the 500-350 °C
642 (Reynolds et al., 1995) and 500-150 °C (Cosca et al., 1991) temperature ranges, suggesting
643 that exhumation was there mainly controlled by post-orogenic erosional unroofing.

644

6. Conclusions

Our combined K-Ar and $^{40}Ar/^{39}Ar$ geochronological and thermochronological study of granites from various portions of the Variscan orogen in western Iberia shows that:

- Granites crystallized at ca. 335 Ma in the Ossa-Morena Zone have recorded mostly ductile stretching (L-tectonites striking around N-S), consistent with N-S extension associated with Variscan intra-orogenic collapse. The small age difference between U-Pb, K-Ar and $^{40}Ar/^{39}Ar$ ages on these granites supports relatively fast cooling associated with rapid tectonic exhumation.
- Deformed granites in the Central Iberian Zone show the highest offset between U-Pb and K-Ar and $^{40}Ar/^{39}Ar$ ages. This supports crystallization at deep level in the core of the chain, followed by a long-cooling history associated with significant exhumation by tectonics processes: fast tectonic exhumation between ca 315 Ma and 285 Ma, due to (1) non purely-horizontal left-lateral movement along shear zones during the end of C3, and (2) late extension during the final collapse of the Variscan orogen (E2).
- Youngest dated granites (crystallization <305 Ma) in both the Ossa-Morena and the Central Iberian zones have recorded mostly isotropic strain (no visible ductile foliation or lineation) and show no significant offset between U/Pb and $^{40}Ar/^{39}Ar$ ages. This supports shallow granite emplacement, during E2, and subsequent low-rate denudation and isostatic rebound.
- Our new K-Ar and $^{40}Ar/^{39}Ar$ data, along with available U-Pb, support a northward propagation of tectonic exhumation from the Ossa-Morena Zone to the Central Iberian Zone.
- Late Carboniferous to early Permian tectonic exhumation was accompanied by significant ore-deposits formation with tin deposits occurring in pegmatites and/or quartz veins associated with the muscovite-rich syn-C3 granites and those of tungsten

occurring in quartz veins, breccia pipes and skarns associated with the E2 biotite-rich granites.

Acknowledgments

Constructive remarks by two reviewers (J.R. Martínez Catalán and anonymous reviewer) and by the Editor helped to significantly improve the quality of the manuscript. Thanks to L. Hughes-Allen for careful reading and useful suggestions regarding the English. This study was supported by research project TEAMINT (POCTI/CTE/48137/2002) and project UIDB/04683/2020-ICT (Institute of Earth Sciences) supported by the Portuguese Foundation for Science and Technology (FCT), and internal funding. This is LGMT contribution 165.

Declaration of interest

The authors declare that they have no known competing financial interests or personal relationships that could have appeared to influence the work reported in this paper.

References

Abalosa, B., Ibarguchi, J.I.G., Eguiluz, L., 1991. Cadomian subduction/collision and Variscan transpression in the Badajoz-Córdoba shear belt, southwest Spain. Tectonophysics, 199, 51-72.

Antic´, M.D., Kounov, A., Trivic´, B., Spikings, R., Wetzel, A., 2017. Evidence of Variscan and Alpine tectonics in the structural and thermochronological record of the central Serbo‐Macedonian Massif (south‐eastern Serbia). Int J Earth Sci (Geol Rundsch) (2017) 106:1665–1692.

Antunes, I. M. H. R. ,Neiva, A.M.R., Corfu, F., 2012. U-Pb Early Ordovician emplacement ages and K-Ar Variscan recrystallization ages of the Fundão granitic pluton, central Portugal. European Mineralogical Conference, Vol. 1, EMC2012-747.

Barbarand, J., Marques, F.O., Hildenbrand, A., Pinna Jamme, R., Nogueira, C.R., 2021. Thermal evolution of onshore west Iberia: towards a better constraint of the age of breakup in the Iberia-Newfoundland Atlantic. Tectonophysics, in revision.

Bea, F., Montero, P., Molina, J.F., 1999. Mafic precursors, peraluminous granitoids, and late lamprophyres in the Avila batholith; a model for the generation of Variscan batholiths in Iberia. J. Geol. 107, 399–419.

Bobos, I., Gonçalves, A.M., Lima, L., Noronha, F., 2019. Micas 40Ar/39Ar dating of hydrothermal events related with the post-orogenic W (±Sn), (Cu, Mo) mineralization from Borralha, Northern Portugal. Life with Ore Deposits on Earth – proceedings of the 15th SGA Biennial Meeting 2019, Glasgow (Scotland) vol 1, 353-356.

Boiron, M.-C., Cathelineau, M., Banks, D.A., Yardley, B., Noronha, F., Miller, M.F., 1996. P-T-X conditions of late Hercynian fluid penetration and the origin of granite-hosted gold quartz veins in northwestern Iberian: a multidisciplinary study of fluid inclusions and their chemistry. Geochim Cosmochim. Acta, 60, 43-57.

712 Burg, J.P., Van den Driessche, Brun, J.P., 1994. Syn- to post-thnickening extension in teh
713 Variscan Belt of Western Europe: Modes and structural consequences. Géologie de la
714 France, 3, 33-51.
715 Capdevila R, Corretge LG, Floor P, 1973. Les granitoïdes Varisques de la Meseta Ibérique.
716 Bull Soc Geol Fr 15: 209-228.
717 Carrilho Lopes, J., Sant'Ovaia, H., Martins, H.C.B., Nogueira, P., Lopes, L., 2016. U-Pb
718 geochronology and Nd isotope contributions to the interpretation of a peculiar ring massif:
719 the Santa Eulália plutonic complex (SW Iberia, Portugal). GEO - Comunicações - Em
720 Congressos Científicos Internacionais 149.

721 Carocci, E., Marignac, C., Cathelineau, M., Truche, L., Lecomte, A., Pinto, F., 2019. Rutile
722 from Panasqueira (Central Portugal): An Excellent Pathfinder for Wolframite Deposition.
723 Minerals 2019, 9, 9; doi:10.3390/min9010009.

724 Cassignol, C., Gillot, P. Y., 1982. Range and effectiveness of unspiked potassium-argon
725 dating: experimental groundwork and applications. Numerical dating in stratigraphy 1,
726 159-179, John Wiley, New York.
727 Chardon, D., Aretz, M., Roques, D., 2020. Reappraisal of Variscan tectonics in the southern
728 French Massif Central. Tectonophysics, 787, 228477.

729 Cherniak, D.J., Watson, E.B., 2000. Pb diffusion in zircon. Chem. Geol., 172, 5-24.
730 Chichorro, M., Pereira, M.F., Díaz-Azpiroz, M., Williams, I.S., Fernández, C., Pin, C., Silva,
731 J.B., 2008. Cambrian ensialic rift-related magmatism in the Ossa-Morena Zone (Évora–
732 Aracena metamorphic belt, SW Iberian Massif): Sm–Nd isotopes and SHRIMP zircon U–
733 Th–Pb geochronology. Tectonophysics, 461, 9-113.
734 Clark AH ,1970. Potassium-argon ages and regional relationships of the Panasqueira
735 tintungsten mineralization. Comun Serv Geol Port 54: 243-261.

736 Cosca, M. A., Sutter, J. F., & Essene, E. J. (1991). Cooling and inferred uplift/erosion history
737 of the Grenville Orogen, Ontario: constraints from $^{40}Ar/^{39}Ar$
738 thermochronology. Tectonics, 10(5), 959-977.
739 Coulié E., X. Quidelleur, J.C. Lefèvre and P.Y. Gillot, 2004. Exploring the multicollection
740 approach for the 40Ar/39Ar dating technique. Geochem. Geophys. Geosyst., 5, Q11010,
741 doi:10.1029/2004GC000773.
742 Dallmeyer R.D., Ribeiro, A., Marques, F.O., 1991. Polyphase Variscan emplacement of
743 exotic terranes (Morais and Bragança Massifs) onto Iberian successions: Evidence
744 from $^{40}Ar/^{39}Ar$ mineral ages. Lithos 27(2), 133-144.
745 Dias, G., Leterrier, J., Mendes, A., Simoes, P.P., Bertrand, J.M., 1998. U–Pb zircon and
746 monazite geochronology of post-collisional Hercynian granitoids from the Central Iberian
747 Zone Northern Portugal. Lithos, ,45, 349-369.
748 Dias, G., Simões, P.P., Ferreira, N., Leterrier, J., 2002. Mantle and crustal sources in the
749 genesis of Late-Hercynian granitoids (NW Portugal): geochemical and Sr-Nd isotopic
750 constraints. Gondwana Res. 5(2), 287–305.
751 Farias, P.; Gallastegui, G.; Gonzalez Lodeiro, F.; Marquinez, J.; Martin Parra, L.M.; Martínez
752 Catalan, J.R.; de Pablo Maciá, J.G.; Rodriguez Fernandez, L.R. 1987. Aportaciones al
753 Conocimiento de la Litoestratigrafia y Estructura de Galícia Central. Mem. Museu
754 Laboratório Mineralogia Geologia da Faculdade Ciências Universidade Porto; 1, 411–431.
755 Ferreira, J.A., Bento dos Santos, T., Pereira, I., Mata, J., 2019. Tectonically assisted
756 exhumation and cooling of Variscan granites in an anatectic complex of the Central Iberian
757 Zone, Portugal: constraints from LA-ICP-MS zircon and apatite U–Pb ages. International
758 Journal of Earth Sciences, 108, 2153–2175.
759 Ferreira, N., Iglésias, M., Noronha, F., Pereira, E., Ribeiro, A., Ribeiro, M.L., 1987.
760 Granitóides da zona Centro-Ibérica e seu enquadramento geodinâmico. In: Bea, F.,

761 Carnicero, A., Gonzalo, J., Lopez-Plaza, M., Rodriguez-Alonso, M. (Eds.), Geologia de los
762 granitoides y rocas asociadas del Macizo Hespérico. Libro Homenage a L.C.G.Figueirola.
763 Editorial Rueda, Madrid, pp. 37–53.

764 Fleck, R.J., Sutter, J.F., Elliot, D.H., 1977. Interpretation of discordant $^{40}Ar/^{39}Ar$ age-spectra
765 of Mesozoic tholeites from Antarctica. Geochem. Cosmochem. Acta, 41, 15-32.

766 Franek, J., Schulmann, K., Lexa, O., Tomek, C., Edel, J.B., 2011. Model of syn-convergent
767 extrusion of orogenic lower crust in the core of the Variscan belt: implications for
768 exhumation of high-pressure rocks in large hot orogens. J. Metamorphic Geol., 29, 53-78,
769 doi.org/10.1111/j.1525-1314.2010.00903.x

770 Franke, W., 2000. The mid-European segment of the Variscides: tectonostratigraphic units,
771 terrane boundaries and plate tectonic evolution. In: Franke, W., Haak, V., Oncken, O.,
772 Tanner, D. (eds), Orogenic Processes: Quantification and Modelling in the Variscan Belt.
773 Geological Society, London, Special Publications 179, 35–61.

774 Fuhrmann, U., Lippolt, H.J., Hess, J.C., 1987. Examination of some proposed K–Ar
775 standards: $^{40}Ar/^{39}Ar$ analyses and conventional K–Ar data. Chemical Geology 66, 41–51.
776 Gébelin, A., Roger, F., Brunel, M., 2009. Syntectonic crustal melting and high-grade
777 metamorphism in a transpressional regime, Variscan Massif Central, France.
778 Tectonophysics, 477, 229-243.
779 Gerbault, M., Schneider, J., Reverso-Peila, A., Corsini, M., 2018. Crustal exhumation during
780 ongoing compression in the Variscan Maures-Tanneron Massif, France-Geological and
781 thermo-mechanical aspects. Tectonophysics, 746, 439-458.
782 Gillot, P.Y. & Cornette, Y., 1986. The Cassignol technique for potassium–argon dating,
783 precision and accuracy — examples from the Late Pleistocene to recent volcanics from
784 southern Italy. Chem. Geol. 59, 205–222.

785 Gillot, P.Y., Cornette, Y., Max, N., Floris, B., 1992. Two reference materials, trachytes
786 MDO-G and ISH-G, for argon dating (K–Ar and Ar-40/Ar-39) of Pleistocene and
787 Holocene rocks. Geostandards Newsletter 16, 55–60.
788 Gillot, P.Y., Hildenbrand, A., Lefevre, J.C., & Albore-Livadie, C., 2006. The K-Ar dating
789 method: principle, analytical techniques, and application to Holocene volcanic eruptions
790 in Southern Italy. Acta Vulcanol. 18, 55–66.
791 Gutiérrez-Alonso G. Fernández-Suárez J., López-Carmona Alicia and Gärtner Andreas, 2018.
792 Exhuming a cold case: The early granodiorites of the northwest Iberian Variscan belt—A
793 Visean magmatic flare-up? LITHOSPHERE; v. 10; no. 2; p. 194–216.
794 Harrison, T. M., Yin, A., Grove, M., Lovera, O. M., Ryerson, F. J., & Zhou, X. (2000). The
795 Zedong Window: A record of superposed Tertiary convergence in southeastern Tibet. J.
796 Geophys. Res. (Solid Earth), 105 (B8), 19211-19230.Hawkesworth, C., Cawood, P.A.,
797 Dhuime, B., 2019. Rates of generation and growth of the continental crust, Geoscience
798 Frontiers 10 (1), doi.org/10.1016/j.gsf.2018.02.004
799 Holmes, A., 1946. An estimate of the age of the Earth. Nature, 157, 680-684.
800 Houtermans, F. G., 1946. Die Isotopenhaüfigkeiten im naturlichen Blei und das Alter des
801 Urans. Naturwiss., 33, p. 185-186.
802 Iglesias, M., Ribeiro, A., 1981. Zones de cisaillement ductile dans l'arc ibéro-armoricain.
803 Comun. Serv. Geol. Port. 67, 85–87.
804 Jaques, L., Noronha, F., Liewig, N., Bobos, I., 2016. Paleofluids circulation associated with
805 the Gerês late-orogenic granitic massif, northern Portugal. Geochemistry, 76 (4), 659-676.
806 Julivert, M., Fontboté, J., Ribeiro, A., Conde, L., 1974. Mapa tectonico de la Penınsula
807 Iberica y Baleares, escala 1/1,000,000. Inst. Geol. Min. Espana, 113 pp.
808 Korchinsky, M., Rey, P.F., Mondy, L., Teyssier, C., Whitney, D.L., 2018. Numerical
809 investigation of deep-crust behavior under lithospheric extension. Tectonophysics 726,

137–146.

Kuiper, K. F., Deino, A., Hilgen, F. J., Krijgsman, W., Renne, P. R., Wijbrans, J. R. (2008). Synchronizing Rock Clocks of Earth History. Science 320: doi: 10.1126/science.1154339. issn: 0036-8075.

Ireland, T.R., Clement, S., Compston, W., Foster, J.J., Holden, P., Jenkins, B., Lanc, P., Schram, N., Williams, I.S., 2008. Development of SHRIMP, Australian Journal of Earth Sciences, 55:6-7, 937-954.

Launay, G., 2018. Hydrodynamique des systèmes minéralisés péri-granitiques : étude du gisement à W-Sn-(Cu) de Panasqueira (Portugal). PhD thesis. Univ. Orléans (France), p. 506.

Lee, J.K.W., Williams, I.S., Ellis, D.J., 1997. Pb, U and Th diffusion in natural zircon. Nature 390, 159–162.

Symposium on Granitic Pegmatites, Bartlett, United States. PEG 2013:77-78.

Lima, S.M., Corfu, F., Neiva, A.M.R., Ramos, J.M.F., 2012. Dissecting Complex Magmatic Processes: an in-depth U-Pb Study of the Pavia Pluton, Ossa^Morena Zone, Portugal. J. Petrol., 53, 9, 1887-1911.

Lima A, Mendes L, Melleton J, Gloaguen E, Frei D, 2013. Seixoso-Vieiros Rare Element Pegmatite Field: Dating the Mineralizing Events. PEG 2013: The 6th International

LNEG, 1992 – Geological map of Portugal scale 1:500,000.

Lopes, J.C., Sant'Ovaia, H., Martins, H.C.B., Nogueira, P., Lopes, L. 2016. U-Pb geochronology and Nd isotope contributions to the interpretation of a peculiar ring massif: the Santa Eulália plutonic complex (SW Iberia, Portugal). Abstracts of the 35th International Geological Congress, Cape Town, South Africa.

Lovera, O.M., Richter, F.M., & Harrison, T.M., 1989. $^{40}Ar/^{39}Ar$ geothermometry for slowly cooled samples having a distribution of diffusion domain sizes. Journal of Geophysical

Research, 94, 17917-17935.

Lovera, O.M., 1992. Computer programs to model $^{40}Ar/^{39}Ar$ diffusion data from multi-domain samples. Computers and Geosciences, 18, 789-813.

Lovera, O.M., Grove, M., Harrison, T.M., & Mahon, K.I., 1997. Systematic analysis of K feldspar Ar/Ar step-heating experiments I: Significance of activation energy determinations. Geochim. Cosmochim. Acta, 61, 3171-3192.

Lee J.K.W., Williams, I.S., Ellis, D.J., 1997. Pb, U and Th diffusion in natural zircon. Nature 390, 159-162.

Marques, F.O., Mateus, A., Tassinari, C., 2002. The Late-Variscan fault network in central–northern Portugal (NW Iberia): a re-evaluation. Tectonophysics 359, 255-270.

Marques de Sá C., Noronha F., Cardellach E., Bobos I. 2019. Fluid inclusion and (S, C, O, Pb) isotope study of Pb-Zn-(Cu-Ag) hydrothermal veins from Central and Northern Portugal – Metallogenic implications. Ore Geology Reviews 112, 1-15

Martínez Catalán, J.R., Rubio Pascual, F.J., Montes, A.D., Fernández, R.D., Barreiro, J.G., Dias Da Silva, Í., Clavijo, E.G., Ayarza, P., Alcock, J.E., 2014. The late Variscan HT/LP metamorphic event in NW and Central Iberia: relationships to crustal thickening, extension, orocline development and crustal evolution. Geological Society, London, Special Publications 405, 225–247.

Marzoli, A., Renne, P. R., Piccirillo, E. M., Ernesto, M., Bellieni, G., & De Min, A. (1999). Extensive 200-million-year-old continental flood basalts of the Central Atlantic Magmatic Province. Science, 284, 616–618.

Mateus, A., Noronha, F., 2010. Sistemas mineralizantes epigenéticos na Zona Centro-Ibérica; expressão da estruturação orogénica Meso-a Tardi-Varisca. Ciências Geológicas-Ensino e Investigação e sua história. Volume II, Geologia Aplicada, 47-61.

859 Matte, P., 1991. Accretionary history and crustal evolution of the Variscan belt in Western
860 Europe. Tectonophysics 196, 309–337.

861 Maurel, O., Respaut, J. P., Monié, P., Arnaud, N., & Brunel, M., 2004. U/Pb emplacement
862 and $^{40}Ar/^{39}Ar$ cooling ages of the eastern Mont-Louis granite massif (Eastern Pyrenees,
863 France). *Comptes Rendus Geoscience*, *336*(12), 1091-1098.

864 McDougall, I., T.M. Harrison, 1999. Geochronology and thermochronology by the $^{40}Ar/^{39}Ar$
865 method, Oxford Univ. Press, New York, 269 pp.

866 Mendes, A., Dias, G., 2004. Mantle-like Sr-Nd isotope composition of Fe-K subalkaline
867 granites: the Peneda-Gerês Variscan massif (NW Iberian Peninsula). Terra Nova, vol. 16,
868 no. 3, pp. 109-115.

869 Moita P, Munhá J, Fonseca P, Tassinari C, Araújo A, Palácios T 2005a).Dating orogenic
870 events in Ossa-Morena Zone. Actas do XIV Semana de Geoquímica/VIII Congresso de
871 Geoquímica dos Países de Língua Portuguesa, 459–462.

872 Moita P, Munhá J, Fonseca P, Tassinari C, Araújo A, Palácios T., 2005b) Phase equilibria and
873 geochronology of Ossa-Morena eclogites. In: XIV Semana de Geoquímica/VIII Congresso
874 de Geoquímica dos Países de Língua Portuguesa. pp 463–466.

875 Moura A, Dória A, Neiva A.M.R, Leal Gomes C, Creaser R.A, 2014. Metallogenesis at the
876 Carris W-Mo-Sn deposit (Gerês, Portugal): Constraints from fluid inclusions, mineral
877 geochemistry, Re-Os and He-Ar isotopes. Ore Geol. Rev., 56:73–93.

878 Murphy, J.B., Quesada, C., Gutiérrez-Alonso, G., Johnston, S.T., Weil, A., 2016. Reconciling
879 competing models for the tectono-stratigraphic zonation of the Variscan orogen in western
880 Europe. Tectonophysics 681, 209–219.

881 Nabelek, P.I., Hofmeister, A.M., Whittington, A.G., 2012. The influence of temperature-
882 dependent thermal diffusivity on the conductive cooling rates of plutons and temperature-
883 time paths in contact aureoles. Earth Planet. Sci. Lett., 317-318, 157-164.

884 Neiva, A. M. R.,1984. Geochemistry of tin-bearing granitic rocks. Chem. Geol., 43, 241-256.

885 Neiva, A. M. R., 2002. Portuguese granites associated with Sn-W and Au mineralizations.
886 Bulletin of the Geological Society of Finland, 74, 79-101.

887 Neiva, A.M.R., Williams, I.S., Lima, S.M., Teixeira, R.J.S., 2012. U–Pb and 39Ar/40Ar data
888 constraining the ages of the source, emplacement and recrystallization/cooling events from
889 late- to post-D3 Variscan granites of the Gouveia area, central Portugal. Lithos, 153, 72–83.

890 Nier, 1A.O., Thompson, R.W., Murphey, B.F., 1941. The isotopic composition of lead and
891 the measurement of geologic Time III. Phys. Rev., 60, 112-116.

892 Nomade, S., Knight, K.B., Beutel, E., Renne, P., 2007. Chronology of the Central Atlantic
893 Magmatic Province: Implications for the Central Atlantic rifting processes and the
894 Triassic–Jurassic biotic crisis. Palaeogeography Palaeoclimatology Palaeoecology, 244 (1),
895 326-344.

896 Noronha, F., Vindel, E., López, J.A., Dória, A., Garcia, E., Boiron, M.-C., Cathelineau, M.,
897 1999. Fluids related to tungsten ore deposits in Northern Portugal and Spanish Central
898 System: a comparative study. Rev. Soc. Geol. España, vol. 12, pp. 397-403.

899 Noronha F., Ribeiro M. A., Almeida A., Dória A., Guedes A., Lima A., Martins H. C,
900 Sant'Ovaia H., Nogueira P., Martins T., Ramos R., Vieira R., 2013. Jazigos filonianos
901 hidrotermais e aplitopegmatíticos espacialmente associados a granitos norte de Portugal. In
902 Geologia de Portugal, Ed: R. Dias, A. Araújo, P. Terrinha & J. C. Kullberg., Escolar
903 Editora Vol I – Geologia Pré-mesozóica de Portugal. pp. 403-438

Noronha, F., 2017. Fluids and Variscan metallogenesis in granite related systems in Portugal. Procedia Earth and Planetary Science, 17, 1-4.

Orejana, D., Villaseca, C., Perez-Soba, C., Lopez-Garcia, J.A., Billstrom, K., 2009. The Variscan gabbros from the Spanish Central System: A case for crustal recycling in the sub-continental lithospheric mantle? Lithos, 110 (1-4), 262-276.

Pereira, I., Dias, R., Bento dos Santos, T., Mata J., 2017. Exhumation of a migmatite complex along a transpressive shear zone: inferences from the Variscan Juzbado–Penalva do Castelo Shear Zone (Central Iberian Zone). J. Geol. Soc. Lond., 174, 1004–1018.

Pereira, M.F., Chichorro, M., Moita, P., Santos, J.F., Solá, A.M.R., Williams, I.S., Silva, J.B., Armstrong, R.A., 2015. The multistage crystallization of zircon in calc‐alkaline granitoids: U–Pb age constraints on the timing of Variscan tectonic activity in SW Iberia. Int J. Earth Sci. (Geol. Rundsch.), 104, 1167–1183.

Pereira, M.F., Díez Fernández, R., Gama, C., Hofmann, M., Gärtner, A., Linnemann, U., 2018. S‐type granite generation and emplacement during a regional switch from extensional to contractional deformation (Central Iberian Zone, Iberian autochthonous domain, Variscan Orogeny), Int. J. Earth. Sci., 107:251–267.

Phillips, D., Matchan, E.L., Honda, M., Kuiper, K.F., 2017. Astronomical calibration of $^{40}Ar/^{39}Ar$ reference minerals using high-precision, multi-collector (ARGUSVI) mass spectrometry. Geochem. Cosmochem. Acta, 196, 351-389.

Priem, H.N.A, den Tex, E., 1984. Tracing crustal evolution in the NW Iberian Peninsula through the Rb/Sr and U-Pb systematics of Palaeozoic granitoids: a review. Physics of the Earth and Planetary Interiors, 35 (1-3), 121-130.

926 Quesada, C., 1991. Geological constraints on the Paleozoic tectonic evolution of
927 tectonostratigraphic terranes in the Iberian Massif. Tectonophysics 185, 225–245.

928 Quidelleur, X., Grove, M., Lovera, O. M., Harrison, T. M., Yin, A., & Ryerson, F. J., 1997.
929 Thermal evolution and slip history of the Renbu Zedong Thrust, southeastern Tibet. J.
930 Geophys. Res. (Solid Earth), 102(B2), 2659-2679.

931 Rackzek, I., Stoll, B., Hofmann, A.W. & Jochum, K.P., 2001. High-precision trace element
932 data for the USGS reference materials BCR-1, BCR-2, BHVO-1, BHVO-2, AGV-1,
933 AGV-2, DTS-1, DTS-2, GSP-1 and GSP-2 by ID-TIMS and MIC-SSMS. Geostandards
934 Newsletter 25, 77-86.

935 Rey, P., Vanderhaeghe, O, Teyssier, C., 2001. Gravitational collapse of the continental crust:
936 definition, regimes and modes. Tectonophysics, 342, 435-449.

937 Reynolds, P. H., Culshaw, N. G., Jamieson, R. A., Grant, S. L., & McKenzie, K. J., 1995.
938 $^{40}Ar/^{39}Ar$ traverse—Grenville Front Tectonic Zone to Britt Domain, Grenville Province,
939 Ontario, Canada. Journal of Metamorphic Geology, 13(2), 209-221.

940 Ribeiro, M.L., Reche, J., López-Carmona, A., Aguilar, A.C., Bento dos Santos, T., Chichorro,
941 M., Dias da Silva, Í., Díez-Montes, A., González-Clavijo, E., Gutiérrez-Alonso, G., Leal,
942 N., Liesa, M., Martínez, F.J., Mateus, A., Mendes, M.H., Moita, P., Pedro, J., Quesada,
943 C., Santos, J.F., Solá, A.R., Valverde-Vaquero, P., 2019. Variscan metamorphism. In C.
944 Quesada and J.T. Oliveira (eds.), The Geology of Iberia: A Geodynamic Approach,
945 Regional Geology Reviews, Springer Nature Switzerland AG 2019.
946 https://doi.org/10.1007/978-3-030-10519-8

947 Ricci J., Quidelleur X., Pavlov V., Orlov S., Shatsillo A. and Courtillot V., 2013. New
948 40Ar/39Ar and K-Ar ages of the Viluy traps (Eastern Siberia): Further evidence for a
949 relationship with the Frasnian-Famennian mass extinction. Palaeogeography,

950 Palaeoclimatology, Palaeoecology, 386, 531-540.

951 Rosas, F., Marques, F., Ballèvre, M., Tassinari, C., 2008. Geodynamic evolution of the SW
952 Variscides: Orogenic collapse shown by new tectonometamorphic and isotopic data from
953 western Ossa-Morena Zone, SW Iberia. Tectonics 27, TC6008, doi:10.1029/
954 2008TC002333.

955 Roth, E., Pothy, B., 1985. Méthodes de datation par les phénomènes nucléaires. Applications.
956 Masson, coll. CEA, 631pp.

957 Sagna I., Quidelleur X., NDiaye F., Gillot P.Y., Lefèvre J.C., Dioh E., 2017. K–Ar mineral
958 ages and thermal history of magmatic and metamorphic Paleoproterozoic units from the
959 northern part of Kedougou inlier, West African Craton (eastern Senegal). Geological
960 Journal, 52, 207-216. DOI: 10.1002/gj.2749.

961 Sagna, I., Quidelleur, X., Dioh, E., Gillot, P. Y., Lefèvre, J. C., Baratoux, L., & Diallo, D. P.,
962 2021. Proterozoic magmatic events recorded in 40Ar/39Ar data from the northern part of
963 the Kedougou Kenieba Inlier (eastern Senegal). *Journal of African Earth Sciences*, *175*,
964 104109.

965 Schwarz, W.H., Trieloff, M., 2007. Intercalibration of $^{40}Ar/^{39}Ar$ age standards NL-25, HB3gr
966 hornblende, GA1550, SB-3, HD-B1 biotite and BMus/2 muscovite. Chemical Geology
967 242, 218–231.

968 Scibiorski, E., Tohver, E., & Jourdan, F., 2015. Rapid cooling and exhumation in the western
969 part of the Mesoproterozoic Albany-Fraser Orogen, Western Australia. Precambrian
970 Research, 265, 232-248.

971 Schermerhorn, L.J.G,1981. Framework and evolution of Hercynian mineralization in the
972 Iberian Meseta. Leidse Geol. Medelelingen 1981, 52, 23–56.

973 Simancas, J.F., Tahiri, A., Azor, A., González Lodeiro, F., Martínez Poyatos, D., El Hadi, H.,

2005. The tectonic frame of the Variscan-Alleghanian Orogen in Southern Europe and Northern Africa. Tectonophysics 398, 181–198.

Snee, L.W., Sutter, J.F., Kelly, W.C., 1988. Thermochronology of economic mineral deposits; dating the stages of mineralization at Panasqueira, Portugal, by high-precision $^{40/39}$Ar age spectrum techniques on muscovite. Economic Geology, 83 (2): 335–354.

Solá, A.R., Williams, I.S., Neiva, A.M.R., Ribeiro, M.L., 2009. U–Th–Pb SHRIMP ages and oxygen isotope composition of zircon from two contrasting late Variscan granitoids, Nisa-Albuquerque batholith, SW Iberian Massif: Petrologic and regional implications. Lithos, 111 (3-4), 156-167.

Steiger, R.H., Jager, E., 1977. Subcommission on geochronology: convention on the use of decay constants in geo and cosmochronology. Earth Planet. Sci. Lett. 36, 359–362.

Tartese, R., Ruffet, G., Poujol, M., Boulvais, P., Ireland, T.R., 2011. Simultaneous resetting of the muscovite K-Ar and monazite U-Pb geochronometers: a story of fluids. Terra Nova, 23 (6), 390-398.

Turillot, P., Augier, R., Monié, P., Faure, M., 2011. Late orogenic exhumation of the Variscan high‐grade units (South Armorican Domain, western France), combined structural and 40Ar/39Ar constraints. Tectonics, 30, doi:10.1029/2010TC002788.

Valle Aguado, B., Azevedo, M.R., Schaltegger, U., Martınez Catalan, J.R., Noland, J., 2005. U–Pb zircon and monazite geochronology of Variscan magmatism related to syn-convergence extension in Central Northern Portugal. Lithos 82, 169–184.

Vanderhaeghe, O., Teyssier, C., 2001. Crustal-scale rheological transitions during late-orogenic collapse. Tectonophysics 335 (1), 211-228.

Vieira, R., Roda-Robles, E., Pesquera, A., Lima, A., 2011. Chemical variation and significance of micas from the Fregeneda-Almendra pegmatitic field (Central-Iberian

Zone, Spain and Portugal). American Mineralogist, 96 (4), 637-645.

Vigneresse J.L., 1999. Intrusion level of granitic massifs along the Hercynian belt: balancing the eroded crust. Tectonophysics, 307, 277-295.

Villaseca, C., Orejana, D., Belousova, E., Armstrong, R.A., Pérez-Soba, C., Jeffries, T.E., 2011. U–Pb isotopic ages and Hf isotope composition of zircons in Variscan gabbros from central Spain: evidence of variable crustal contamination. Miner. Petrol., 101, 151–167.

Zhang, R.Q., Ramos, V., Leal, S., Noronha, F., Pinto, F., 2019. U-Pb geochronology of cassiterites from primary Sn mineralizations in Sn-W Variscan Metallogenic Province, Portugal. Life with ore deposits on Earth, Proceedings of the 15th SGA biennal Meeting, Glasgow (Scotland), 357-360.

Table captions:

Table 1: Main characteristics of the investigated outcrops and samples. OMZ – Ossa-Morena Zone; CIZ – Central Iberian Zone; GTMZ – Galicia Trás-os-Montes Zone. Symbols and description according to the geological map of Portugal (1/500,000 Geological map of Portugal-LNEG (1992). Zircon U-Pb ages from: (1) Chichorro et al. (2008); (2) Pereira et al. (2015); (3) Lima et al. (2012); (4) Sola et al. (2009); (5) Lopes et al. (2016); (6) Antunes et al.

(2012); (7) Neiva et al., 2012; (8) Valle-Aguado et al. (2005); (9) Ferreira et al. (2019); (10) Pereira et al. (2018); (11) Dias et al. (1998). Pre-Variscan ages (inherited zircon) indicated in Italics. Additional information on previous U/Pb ages is provided in Supplement 1.

Table 2: New K-Ar results on the various mineral phases of our samples. Lat.: latitude, Long.: longitude; KFd: K-Feldspar (only one Ar determination), biot: biotite, musc: muscovite. The mean age is obtained by weighing by the amount of radiogenic argon (^{40}Ar*), except in the case of 107D-biot, 107G-biot, and 107J-musc; for the latter, all three individual determinations overlap within uncertainties, and the mean age (*) is calculated by weighing by the inverse of variance. Measured ages in normal font, and mean ages in bold font. Uncertainties quoted at the 1σ level.

Table 3: New ^{40}Ar/^{39}Ar results on the various mineral phases of our samples. Plateau ages are given with analytical uncertainties, with the total (i.e. including J-factor error) uncertainty in parentheses. n: number of steps included in the plateau; N: total number of steps performed. % ^{39}Ar: cumulative amount of ^{39}Ar included in the plateau. MSWD: mean square weighted deviates. All uncertainties quoted at the 1σ level.

Figure captions:

Figure 1: Simplified geological map of Portugal showing the various Variscan and pre-Variscan chrono-stratigraphic units in the main tectonic zones. The position of our dated samples is reported with black circles. Sample acronyms indicated with bold italic font. SPZ is South Portuguese Zone, and GTMZ is Galicia–Trás-os-Montes Zone. Main towns shown with dark blue solid squares; smaller towns and villages shown with white squares

1045 circled with black. A: Alpalhão, CM: Campo Maior, F: Fundão, G: Guimarães, M: Monforte,
1046 P: Pavia, V: Vendinha.

1047

1048 Figure 2: Tectonic/metamorphic/igneous evolution in the CIZ, GTMZ and OMZ. C stands for
1049 contractional deformation, E for extensional, M for metamorphic, and I for igneous. I1 – Syn-
1050 kinematic gabbro, granodiorite, and tonalite; I2 – syn-kinematic granite and adamellite; I3 –
1051 late- to post-kinematic granitoids. Metamorphic grades, tectonic events, and some of the ages
1052 from Martínez Catalán et al. (2014). Subduction to collision age from Moita et al. (2005a, b).
1053 I1 ages 360-330 Ma from Dallmeyer et al. (1993), Rosas et al. (2008), Jesus et al. (2007), Pin
1054 et al. (2008).

1055

1056 Figure 3: $^{40}Ar/^{39}Ar$ age spectra on biotite and muscovite. Plateau ages shown with double
1057 arrows. Total age uncertainty in brackets.

1058

1059 Figure 4: Comparison between our K-Ar and $^{40}Ar/^{39}Ar$ integrated ages.

1060

1061 Figure 5: $^{40}Ar/^{39}Ar$ age spectra on K-Feldspars of our samples.

1062

1063 Figure 6: Comparison of thermal histories obtained for samples 107AC and 107AS with
1064 MDD inverse and forward modelling (all using an imposed activation energy of 46 kcal/mol,
1065 see supplementary figures 1 and 2 for more detail). Note the overall good agreement between
1066 inverse and forward modelling for each sample.

Figure 7: Comparison of the 4 thermal histories obtained with MDD forward modelling on K-Feldspars of our samples 107J, X, AC and AS (all using an imposed activation energy of 46 kcal/mol; Lovera et al., 1997).

Figure 8: Comparison between our K-Ar ages on biotite and available U-Pb age on zircons.

Figure 9: Comparison of our new K/Ar and $^{40}Ar/^{39}Ar$ ages on micas and available U-Pb on zircons (see references in Table 1). The new ages acquired on biotite and muscovite are shown with black and brown characters, respectively. JPCSZ: Juzbado-Penalva do Castelo Shear Zone; JPCSZ: Juzbado-Penalva do Castelo Shear Zone ; CBCSZ - Coimbra-Badajoz-Cordoba Shear Zone.

Figure 10: Synthetic cartoon showing the successive vertical positions of samples J, X, AC and AS between 300 and 250 Ma, as deduced from MDD modelling. Sample 107AS is a granite intruded into the nappes of the GTMZ (after thrusting). F1: main thrust separating the South Portuguese Zone (SPZ) and the Ossa-Morena Zone (OMZ); F2: Coimbra-Badajoz-Cordoba Shear Zone (CBCSZ) separating the Ossa-Morena Zone and the Central Iberian Zone; F3: Juzbado-Penalva do Castelo Shear Zone (JPCSZ). Solid lines indicate inferred active fault movements at a given time; dotted lines indicate inactive fault movements. In each structural zone, colored arrows, show the amount of uplift between successive stages.

Sample	Longitude (°)	Latitude (°)	Zone	Symbol – description on the geological map	Amount of strain	Strain type – kinematics *Field data*	U-Pb (Ma)
107D	38.46046	-7.75290	OMZ	pe_{mg} – Proterozoic series migmatized Variscan orogeny	+++	Pervasive steep foliation strike N160	*577 ± 10 (1)* 341 ± 2 (2)
107G	38.48016	-7.64957	OMZ	t – orogenic tonalite	+ +	L-tectonite with lineation strike N170 Late sinistral strike-slip E-W fault	329 ± 1 (3)
107J	38.84073	-7.89542	OMZ	γ – orogenic biotite-rich granite	+	Weak foliation strike N120	323 ± 1 (3)
107K	39.08173	-7.41841	OMZ	γ3 – late-orogenic biotite-rich porphyroid granite	no	Isotropic	305 ± 6 (4) 301 ± 5 (5)
107P	38.98935	-7.14817	OMZ	T1 – orogenic anorthosite gabbro	no	Isotropic	305 ± 6 (4)
107T	39.41024	-7.62334	CIZ	γ3 – late-orogenic porphyroid monzonite granite	no	Isotropic	305 ± 6 (4)
107X	40.17919	-7.48563	CIZ	γII 2a – syn-tectonic quartzdiorite and biotite granite	no	Heavily fractured	*478 ± 0.5 (6)* 310 ± 4 (7)
107AC	40.76379	-6.85296	CIZ	Monzonite granite with sparse feldspar megacrysts; muscovite and biotite granite	no	Fractured	303 ± 7 (7)
107AH2	40.84370	-7.18323	CIZ	γ1T – orogenic augen gneiss	+++	Pervasive foliation, sub-vertical E-W ductile shear zone, sinistral kinematics	313 - 317 Ma (8,9)
107AJ	40.99665	-7.47315	CIZ	γI3 – syn-F3 orogenic 2-mica granite	++	Ductile, sub-vertical foliation N135 (S), N100 sub-vertical (C), lineation 15º, N100, left-lateral kinematics	319 ± 3 (10)
107AN	41.08813	-7.79960	CIZ	γII1 – early orogenic biotite granodiorite	++	Ductile, foliation N070, 55ºSE Dykes N015, 25ºE cut by faults N45, 55ºSE striation 45°, N160, normal dextral kinematics	319 ± 4 (11)
107AS	41.50952	-8.25861	GTMZ	γII 2b (γII3c?) – syn-orogenic porphyroid granite/granodiorite	+	Faults N060 sub-vertical, sinistral strike-slip Faults N020, sub-vertical, dextral strike-slip	309 ± 1 (11)

Table 1. Main characteristics of the investigated outcrops and samples. OMZ – Ossa-Morena Zone; CIZ – Central Iberian Zone; GTMZ – Galicia Trás-os-Montes Zone. Symbols and description according to the geological map of Portugal (1/500,000 Geological map of Portugal-LNEG (1992). Zircon U-Pb ages from: (1) Chichorro et al. (2008); (2) Pereira et al. (2015); (3) Lima et al. (2012); (4) Sola et al. (2009); (5) Lopes et al. (2016); (6) Antunes et al. (2012); (7) Neiva et al., 2012; (8) Valle-Aguado et al. (2005); (9) Ferreira et al. (2019); (10) Pereira et al. (2018); (11) Dias et al. (1998). Pre-Variscan ages (inherited zircon) indicated in Italics. Additional information on previous U/Pb ages is provided in Supplement 1.

Table 2. New K-Ar results on the various mineral phases of our samples. Lat.: latitude, Long.: longitude; KFd: K-Feldspar (only one Ar determination), biot: biotite, musc: muscovite. The mean age is obtained by weighing by the amount of radiogenic argon ($^{40}Ar^*$), except in the case of 107D-biot, 107G-biot, and 107J-musc; for the latter, all three individual determinations overlap within uncertainties, and the mean age (*) is calculated by weighing by the inverse of variance. Measured ages in normal font, and mean ages in bold font. Uncertainties quoted at the 1σ level.

Sample	**Longitude**	**Latitude**	**K%**	**$^{40}Ar^*$ (%)**	**$^{40}Ar^*$ (10^{15} at.g^{-1})**	**Age (Ma)**	**Unc. (Ma)**
107D-biot	-7.75290	38.46046	7.598	98.7	2.918	334.6	4.7
				99.2	2.943	337.2	4.8
				97.9	2.903	333.1	4.7
					mean*	**335.0**	**2.7**
107G-biot	-7.64957	38.48016	7.643	98.4	2.927	333.8	4.7
				98.6	2.850	325.8	4.6
				96.5	2.889	329.8	4.7
					mean*	**329.7**	**2.7**
107J-biot	-7.89542	38.84073	7.471	97.3	2.722	318.9	4.5
				95.7	2.619	307.8	4.4
				99.3	2.663	312.5	4.4
					mean	**313.0**	**4.4**
107J-musc	-7.89542	38.84073	8.722	97.2	3.095	311.3	4.4
				98.9	3.122	313.8	4.4
				98.7	3.102	311.9	4.4
					mean*	**312.3**	**2.6**
107K-biot	-7.41841	39.08173	6.808	98.9	2.356	304.2	4.3
				96.9	2.363	305/0	4.3
					mean	**304.6**	**4.3**
107J-KFd	-7.89542	38.84073	10.050	94.1	3.273	287.6	4.1
107P-biot	-7.14817	38.98935	7.725	98.9	2.685	305.4	4.3
				98.5	2.706	307.6	4.4
					mean	**306.5**	**4.3**
107T-KFd	-7.62334	39.41024	10.890	96.3	3.319	270.5	3.8
107T-biot	-7.62334	39.41024	7.494	97.8	2.549	299.4	4.2
				97.5	2.509	295.1	4.2
					mean	**297.3**	**4.2**

107T-musc	-7.62334	39.41024	7.928	98.0	2.714	301.2	4.3
				98.1	2.732	303.0	4.3
					mean	**302.1**	**4.3**
107X-KFd	-7.48563	40.17919	11.308	88.0	3.355	263.8	3.7
107X-biot	-7.48563	40.17919	7.692	98.9	2.492	286.3	4.1
				98.6	2.533	290.6	4.1
					mean	**288.4**	**4.1**
107AC-KFd	-6.85296	40.76379	8.819	96.1	2.683	270.0	3.8
107AC-biot	-6.85296	40.76379	7.335	98.0	2.491	299.0	4.2
				92.2	2.464	296.0	4.2
					mean	**297.4**	**4.2**
107AC-musc	-6.85296	40.76379	8.266	97.7	2.811	299.3	4.2
				95.7	2.723	290.7	4.1
				98.5	2.738	292.1	4.1
					mean	**294.0**	**4.2**
107AH2-biot	-7.18323	40.84370	7.561	97.8	2.482	289.8	4.1
				98.3	2.560	298.1	4.2
					mean	**294.0**	**4.2**
107AJ-biot	-7.47315	40.99665	7.521	99.1	2.491	292.1	4.1
				98.6	2.451	287.8	4.1
					mean	**289.9**	**4.1**
107AN-biot	-7.79960	41.08813	7.371	92.2	2.553	304.4	4.3
				98.9	2.606	310.3	4.4
				98.8	2.502	298.8	4.2
					mean	**304.5**	**4.3**
107AS-biot	-8.25861	41.50952	7.640	93.4	2.691	309.1	4.4
				97.9	2.671	307.1	4.4
					mean	**308.1**	**4.4**

Table 3. New $^{40}Ar/^{39}Ar$ results on the various mineral phases of our samples. Plateau ages are given with analytical uncertainties, with the total (i.e. including J-factor error) uncertainty in parentheses. n: number of steps included in the plateau; N: total number of steps performed. % ^{39}Ar: cumulative amount of ^{39}Ar included in the plateau. MSWD: mean square weighted deviates. All uncertainties quoted at the 1σ level.

Sample	Plateau age (Ma)	n/N	(% ^{39}Ar)	MSWD	Integrated age (Ma)	K-Ar age (Ma)
107J-biot	-	-	-	-	309.2 ± 2.9	313.0 ± 4.4
107J-musc	308.7 ± 0.2 (2.8)	8/13	83.8	2.1	308.8 ± 3.0	312.2 ± 2.6
107T-biot	297.1 ± 0.2 (2.7)	4/11	52.5	1.2	295.7 ± 2.8	297.3 ± 4.2
107T-musc	297.1 ± 0.2 (2.8)	6/14	70.0	1.9	297.2 ± 2.8	302.1 ± 4.3
107AC-biot	296.4 ± 0.3 (2.7)	5/13	51.8	1.5	294.1 ± 2.8	297.4 ± 4.2
107AC-musc	294.5 ± 0.1 (2.7)	11/15	92.1	2.3	294.9 ± 2.8	294.0 ± 2.4
107X-biot	-	-	-	-	283.7 ± 2.8	288.4 ± 4.1
107AN-biot	300.4 ± 0.2 (2.8)	5/11	51.8	3.0	298.6 ± 2.8	304.5 ± 4.3
107AS - biot	-	-	-	-	304.2 ± 2.9	308.1 ± 4.4
107J - KFd	-	-	-	-	281.0 ± 2.7	287.6 ± 4.1 *
107T - KFd	-	-	-	-	272.6 ± 2.7	270.5 ± 3.8 *
107X - KFd	-	-	-	-	265.6 ± 2.6	263.8 ± 3.7 *
107AC - KFd	-	-	-	-	261.0 + 2.6	270.0 ± 3.8 *
107AC - KFd-duplicate	-	-	-	-	261.3 ± 2.6	270.0 ± 3.8 *
107AS - KFd	-	-	-	-	292.3 ± 2.6	

Figure 1

Click here to access/download;Figure (with caption below and on the same page);Figure1-R1.jpg

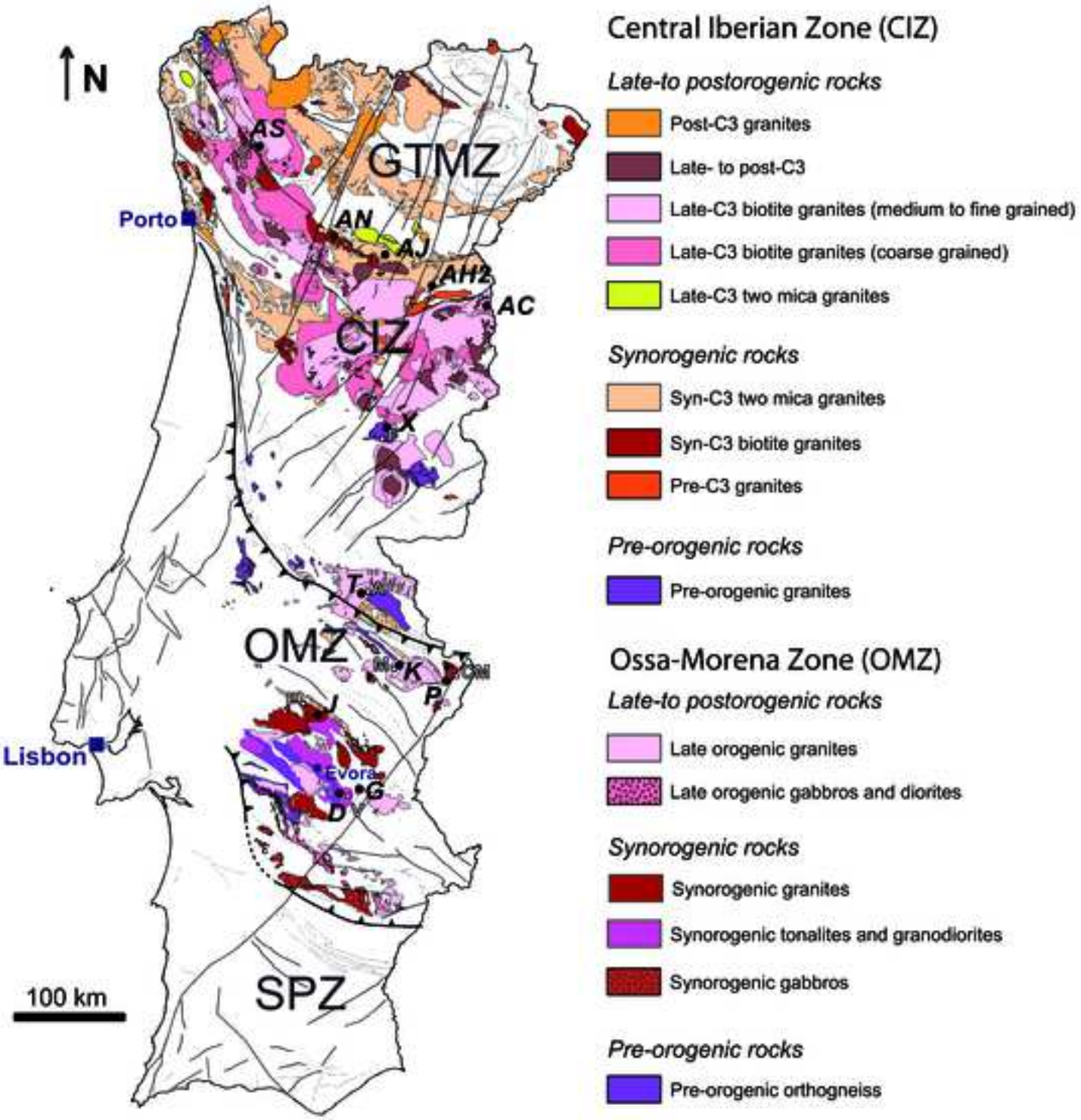

Figure 1: Simplified geological map of Portugal showing the various Variscan and pre-Variscan chrono-stratigraphic units in the main tectonic zones. The position of our dated samples is reported with black circles. Sample acronyms indicated with bold italic font. SPZ is South Portuguese Zone, and GTMZ is Galicia–Trás-os-Montes Zone. Main towns shown with dark blue solid squares; smaller towns and villages shown with white squares circled with black. A: Alpalhão, CM: Campo Maior, F: Fundão, G: Guimarães, M: Monforte, P: Pavia, V: Vendinha.

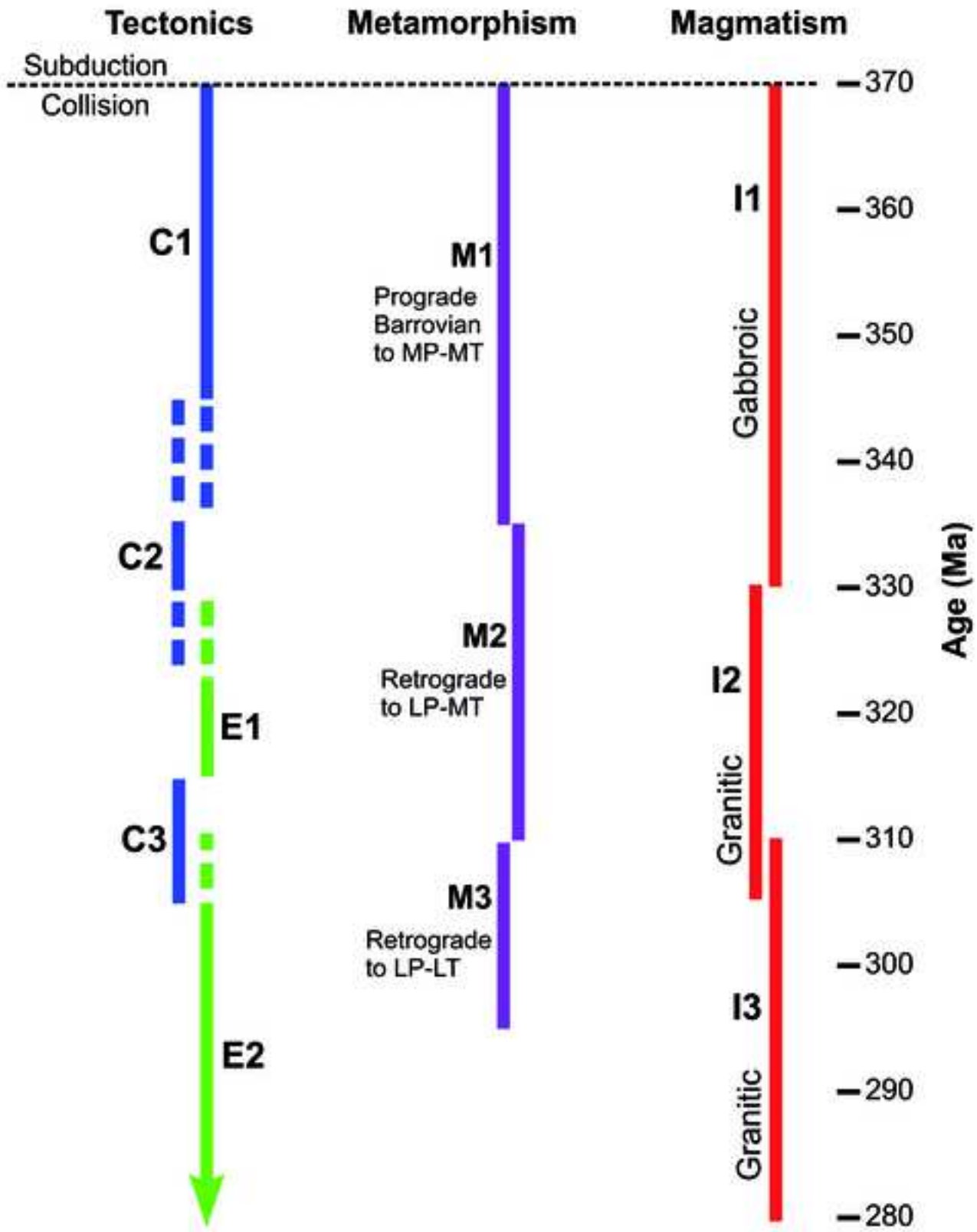

Figure 2: Tectonic/metamorphic/igneous evolution in the CIZ, GTMZ and OMZ. C stands for contractional deformation, E for extensional, M for metamorphic, and I for igneous. I1 – Syn-kinematic gabbro, granodiorite, and tonalite; I2 – syn-kinematic granite and adamellite; I3 – late- to post-kinematic granitoids. Metamorphic grades, tectonic events, and some of the ages from Martínez Catalán et al. (2014). Subduction to collision age from Moita et al. (2005a, b). I1 ages 360-330 Ma from Dallmeyer et al. (1993), Rosas et al. (2008), Jesus et al. (2007), Pin et al. (2008).

Figure 3

Click here to access/download;Figure (with caption below and on the same page);Figure3-R1.jpg

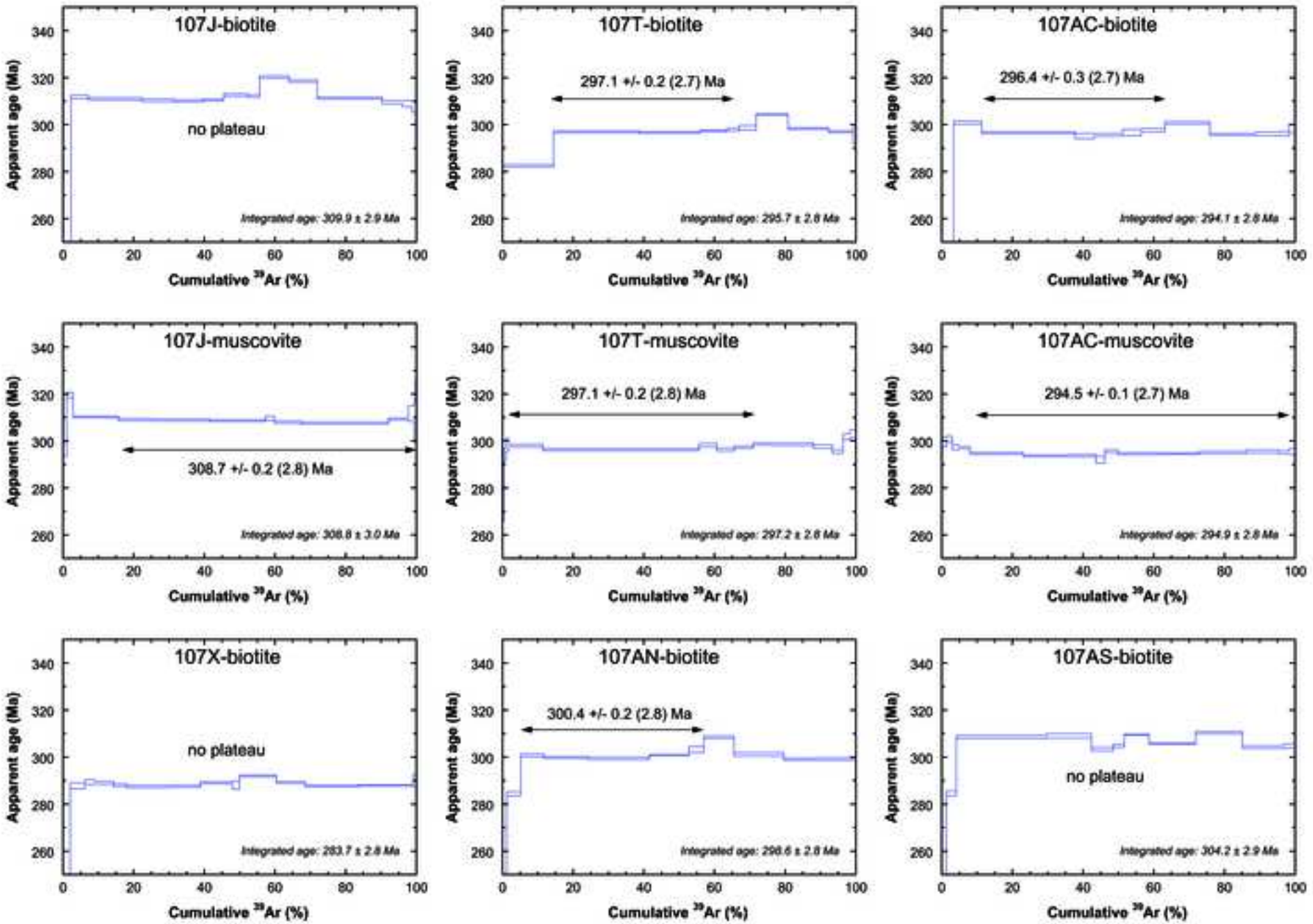

Figure 3: $^{40}Ar/^{39}Ar$ age spectra on biotite and muscovite. Plateau ages shown with double arrows. Total age uncertainty in brackets.

Figure 4

Click here to access/download;Figure (with caption below and on the same page);Figure4-R1.jpg

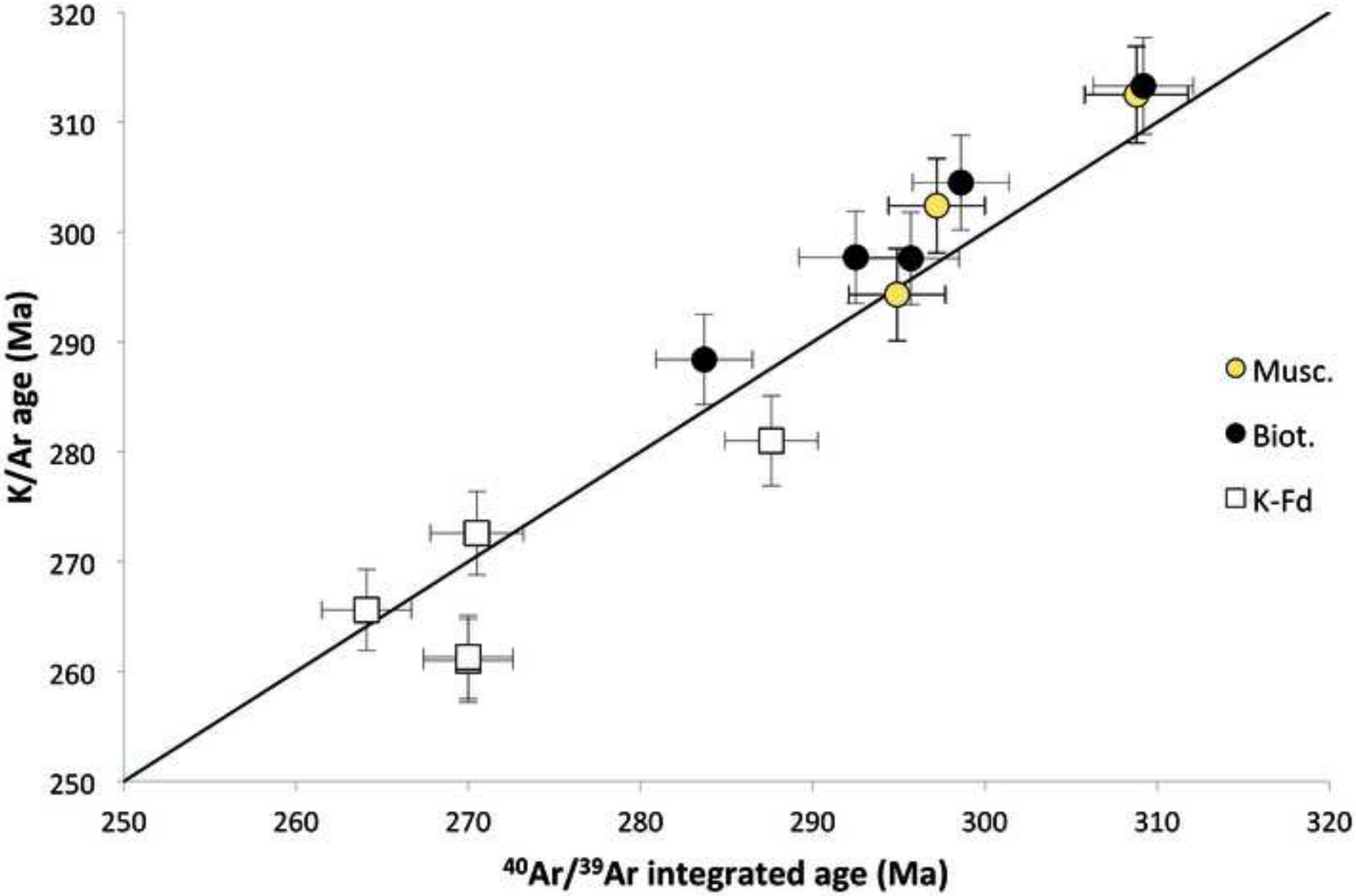

Figure 4: Comparison between our K-Ar and $^{40}Ar/^{39}Ar$ integrated ages.

Figure 5

Click here to access/download;Figure (with caption below and on the same page);Figure5-R1.jpg

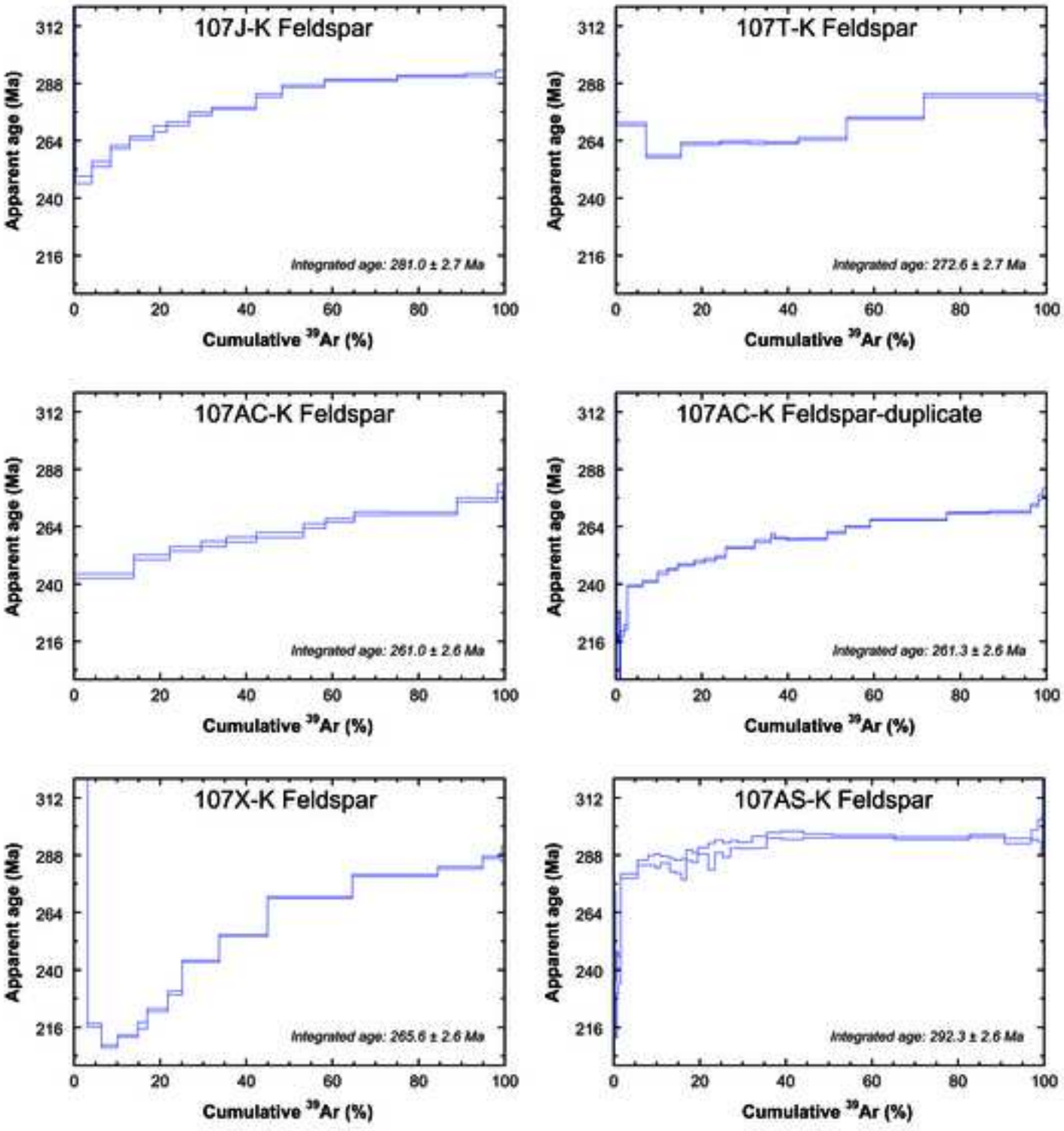

Figure 5: $^{40}Ar/^{39}Ar$ age spectra on K-Feldspars of our samples.

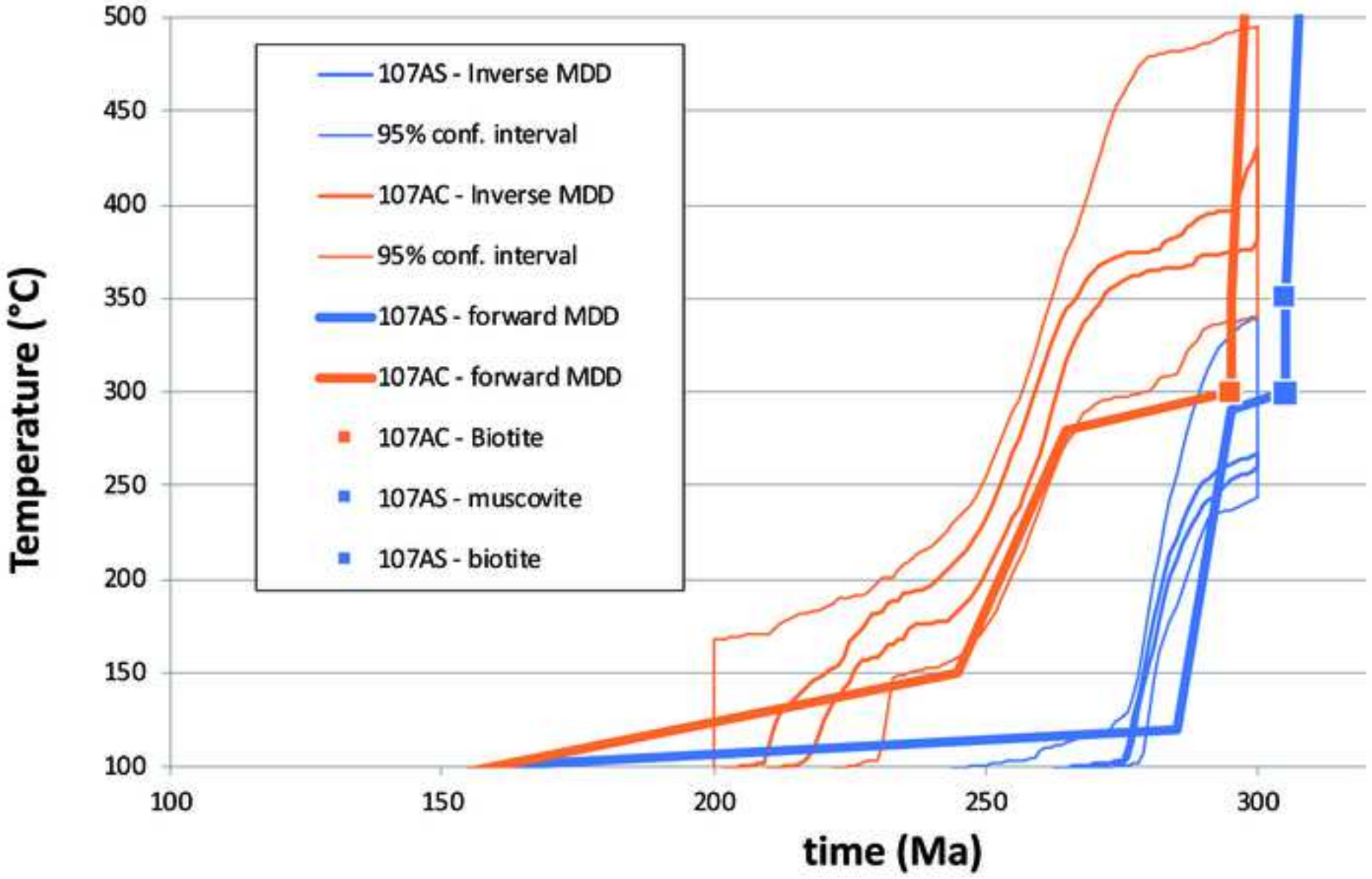

Figure 6: Comparison of thermal histories obtained for samples 107AC and 107AS with MDD inverse and forward modelling (all using an imposed activation energy of 46 kcal/mol, see supplementary figures 1 and 2 for more detail). Note the overall good agreement between inverse and forward modelling for each sample.

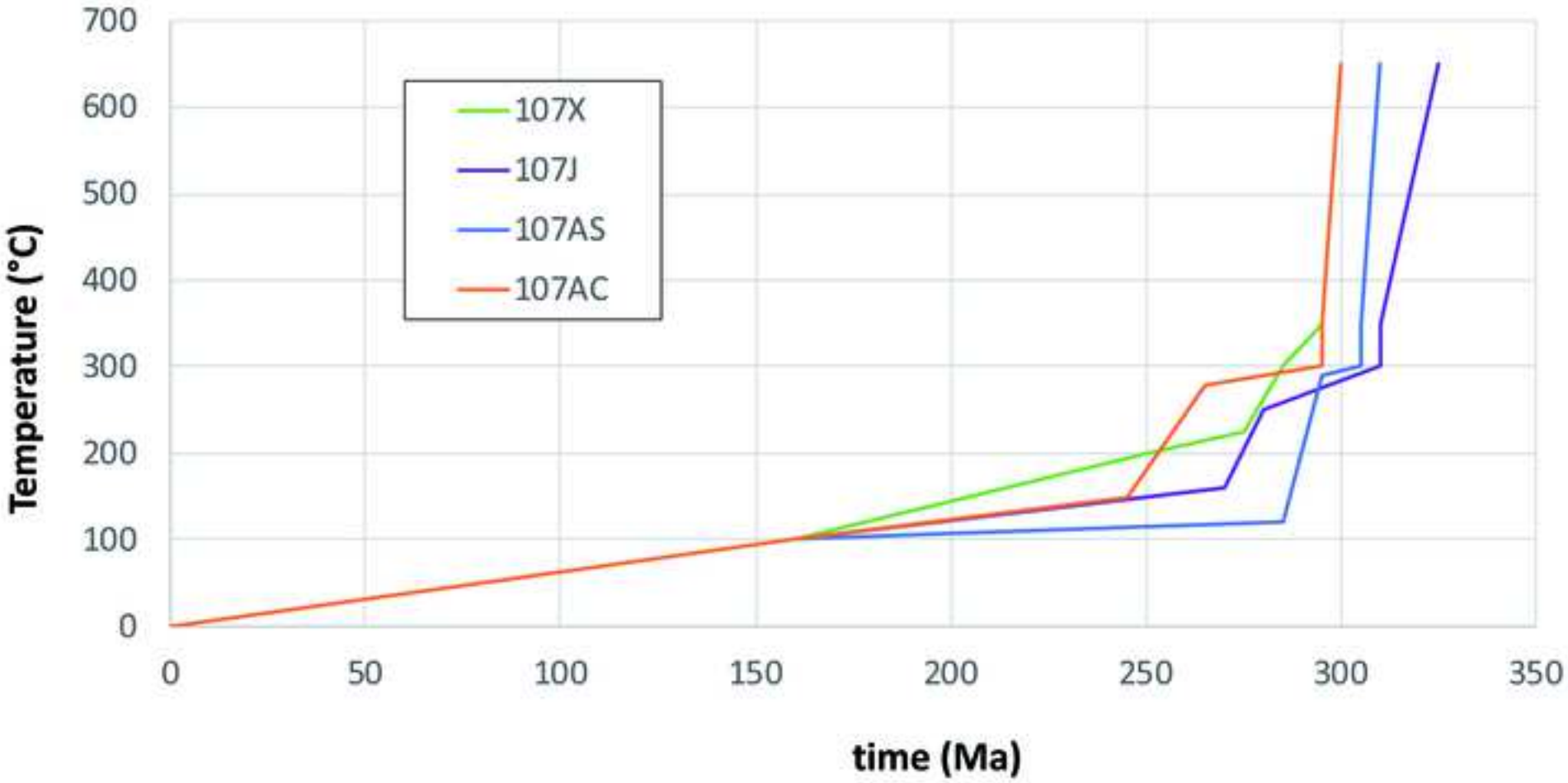

Figure 7: Comparison of the 4 thermal histories obtained with MDD forward modelling on K-Feldspars of our samples 107J, X, AC and AS (all using an imposed activation energy of 46 kcal/mol; Lovera et al., 1997).

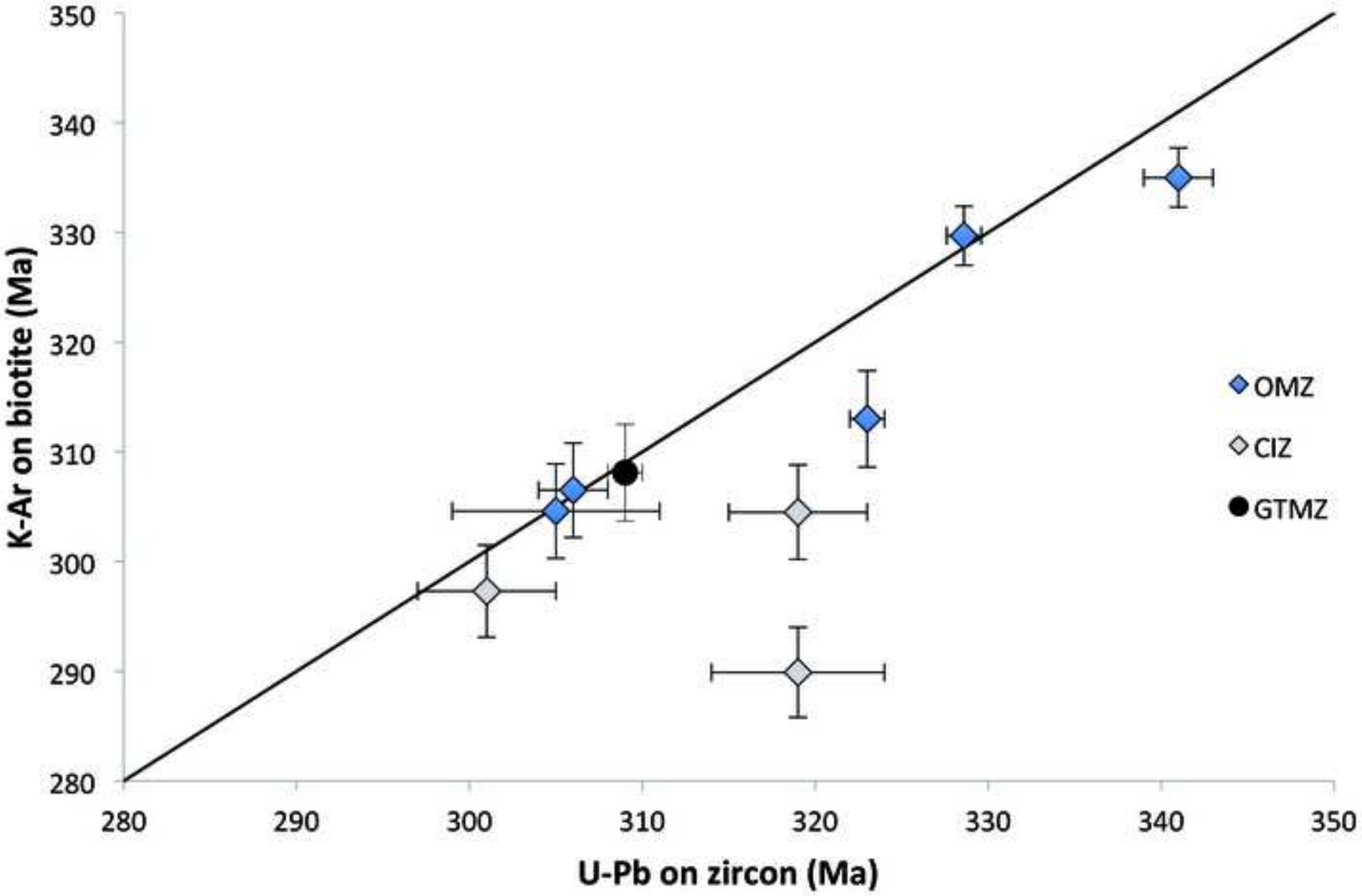

Figure 8: Comparison between our K-Ar ages on biotite and available U-Pb age on zircons.

Figure 9

Click here to access/download;Figure (with caption below and on the same page);Figure9-R1.jpg

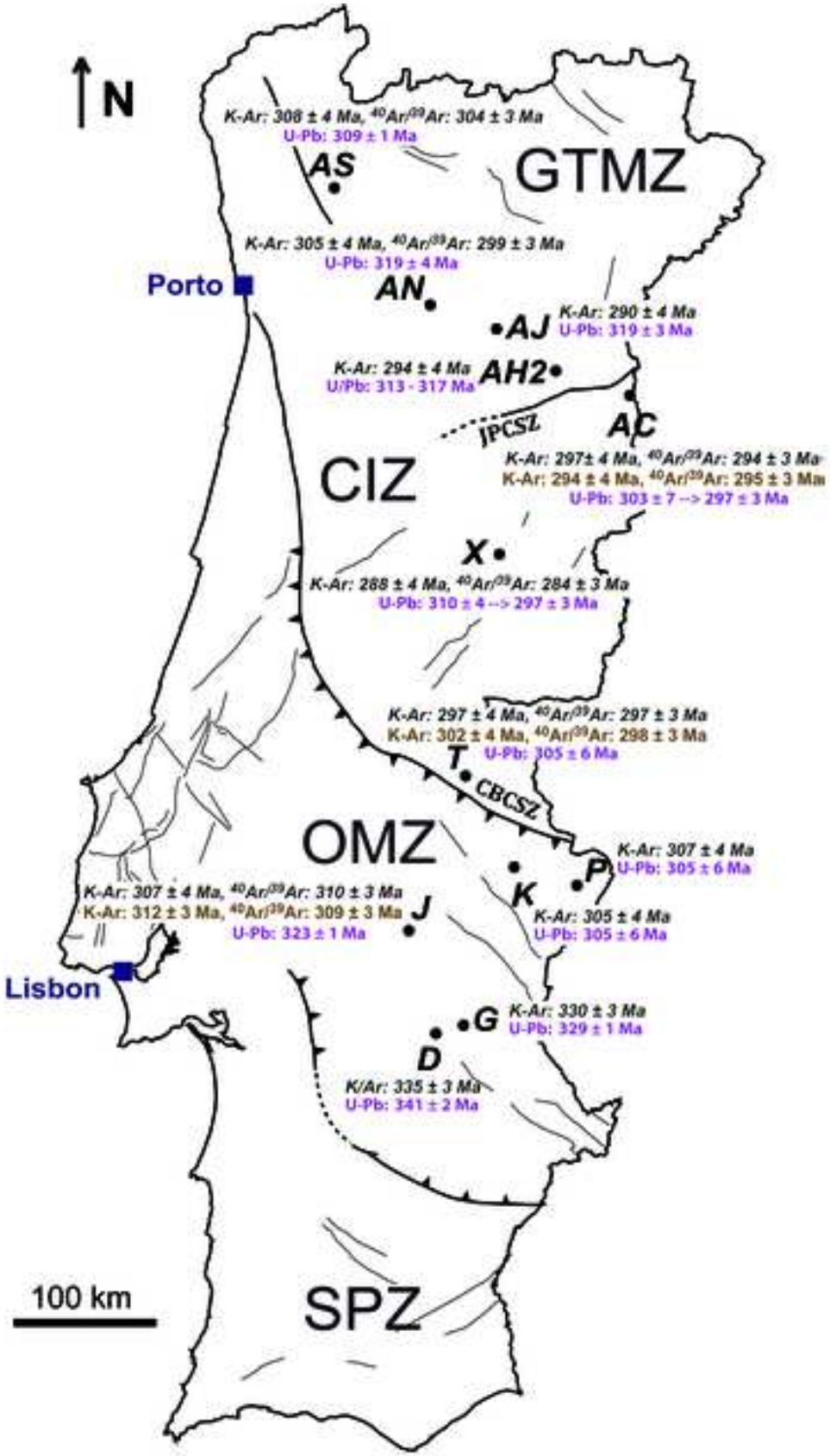

Figure 9: Comparison of our new K/Ar and $^{40}Ar/^{39}Ar$ ages on micas and available U-Pb on zircons (see references in Table 1). The new ages acquired on biotite and muscovite are shown with black and brown characters, respectively. JPCSZ: Juzbado-Penalva do Castelo Shear Zone; JPCSZ: Juzbado-Penalva do Castelo Shear Zone ; CBCSZ - Coimbra-Badajoz-Cordoba Shear Zone.

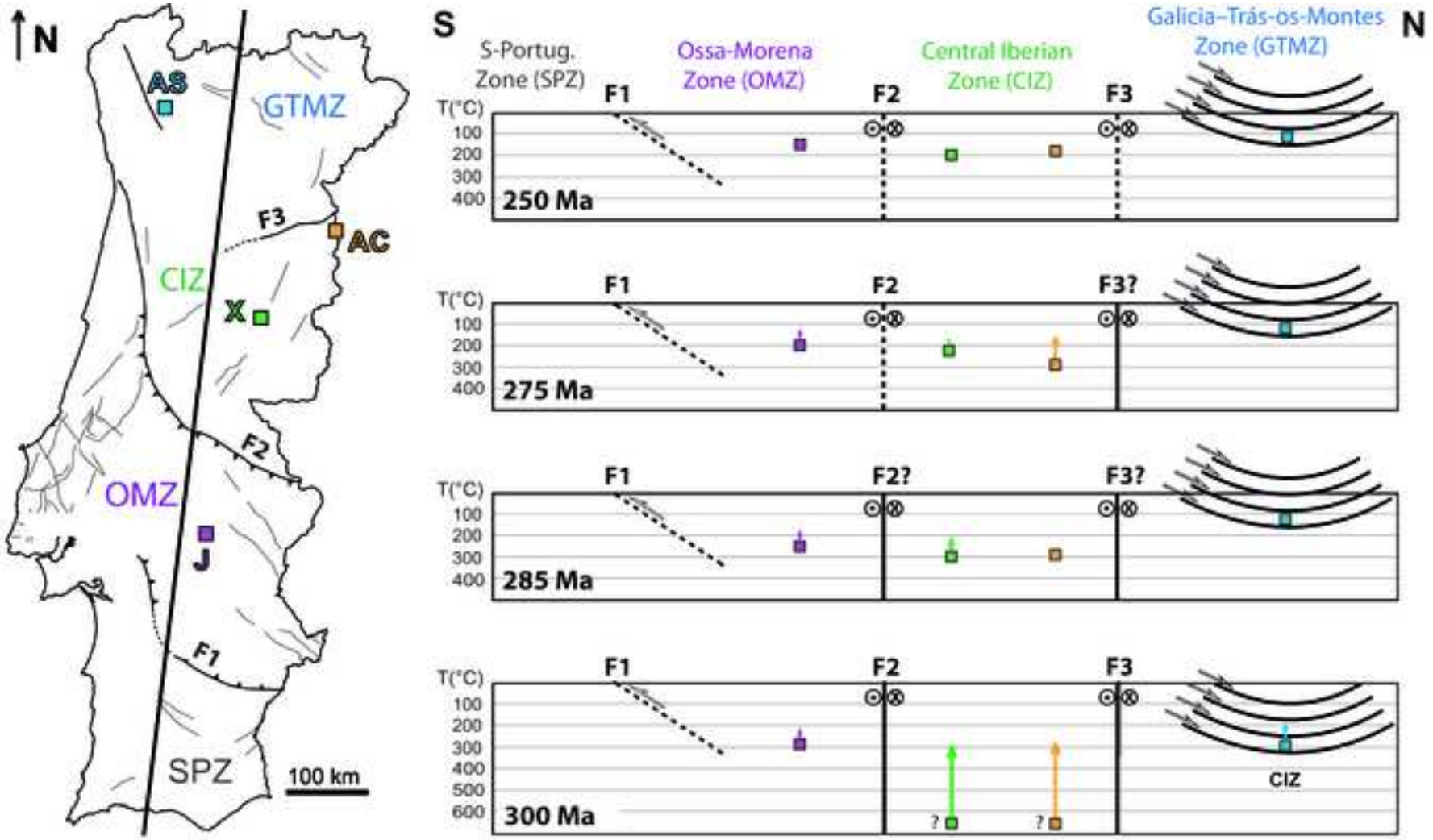

Figure 10: Synthetic cartoon showing the successive vertical positions of samples J, X, AC and AS between 300 and 250 Ma, as deduced from MDD modelling. Sample 107AS is a granite intruded into the nappes of the GTMZ (after thrusting). F1: main thrust separating the South Portuguese Zone (SPZ) and the Ossa-Morena Zone (OMZ); F2: Coimbra-Badajoz-Cordoba Shear Zone (CBCSZ) separating the Ossa-Morena Zone and the Central Iberian Zone; F3: Juzbado-Penalva do Castelo Shear Zone (JPCSZ). Solid lines indicate inferred active fault movements at a given time; dotted lines indicate inactive fault movements. In each structural zone, colored arrows, show the amount of uplift between successive stages.

Supplement 1

Supplementary Figures 1 to 5

Supplementary data (40Ar/39Ar)

Declaration of interests

The authors declare that they have no known competing financial interests or personal relationships that could have appeared to influence the work reported in this paper.

Credit Authors statement

Anthony Hildenbrand (AH) and Fernando Ornelas Marques (FOM) designed the study. **AH** and **Xavier Quidelleur (XQ)** achieved the geochronological and thermochronological analyses. **Fernando Noronha (FN)** supervised the aspects regarding minearlization processes. All authors (AH, FOM, XQ, FN) contributed to drafting and discussion.